

Molecular Physics

An International Journal at the Interface Between Chemistry and Physics

ISSN: (Print) (Online) Journal homepage: <https://www.tandfonline.com/loi/tmph20>

Cross-polarisation ENDOR for spin-1 deuterium nuclei

Isabel Bejenke, Robert Zeier, Roberto Rizzato, Steffen J. Glaser & Marina Bennati

To cite this article: Isabel Bejenke, Robert Zeier, Roberto Rizzato, Steffen J. Glaser & Marina Bennati (2020) Cross-polarisation ENDOR for spin-1 deuterium nuclei, Molecular Physics, 118:18, e1763490, DOI: [10.1080/00268976.2020.1763490](https://doi.org/10.1080/00268976.2020.1763490)

To link to this article: <https://doi.org/10.1080/00268976.2020.1763490>



© 2020 The Author(s). Published by Informa UK Limited, trading as Taylor & Francis Group



Published online: 12 Jun 2020.



Submit your article to this journal [↗](#)



Article views: 446



View related articles [↗](#)



View Crossmark data [↗](#)

RESEARCH ARTICLE



Cross-polarisation ENDOR for spin-1 deuterium nuclei

Isabel Bejenke^a, Robert Zeier^{b,c}, Roberto Rizzato^{a†}, Steffen J. Glaser^{b,d} and Marina Bennati^{a,e}

^aResearch Group EPR Spectroscopy, Max Planck Institute for Biophysical Chemistry, Göttingen, Germany; ^bDepartment of Chemistry, Technical University of Munich, Garching, Germany; ^cQuantum Control (PGL-8), Peter Grünberg Institute, Forschungszentrum Jülich GmbH, Jülich, Germany; ^dMunich Center for Quantum Science and Technology (MCQST), München, Germany; ^eDepartment of Chemistry, Georg-August-Universität Göttingen, Göttingen, Germany

ABSTRACT

Efficient transfer of spin polarisation from electron to nuclear spins is emerging as a common target of several advanced spectroscopic experiments, ranging from sensitivity enhancement in nuclear magnetic resonance (NMR) and methods for the detection of single molecules based on optically detected magnetic resonance (ODMR) to hyperfine spectroscopy. Here, we examine the feasibility of electron-nuclear cross-polarisation at a modified Hartmann-Hahn condition (called eNCP) for applications in ENDOR experiments with spin-1 deuterium nuclei, which are important targets in studies of hydrogen bonds in biological systems and materials. We have investigated a two-spin model system of deuterated malonic acid radicals in a single crystal. Energy matching conditions as well as ENDOR signal intensities were determined for a spin Hamiltonian under the effect of microwave and radiofrequency irradiation. The results were compared with numerical simulations and 94-GHz ENDOR experiments. The compelling agreement between theoretical predictions and experimental results demonstrates that spin density operator formalism in conjunction with suitable approximations in regard to spin relaxation provides a satisfactory description of the polarisation transfer effect. The results establish a basis for future numerical optimizations of polarisation transfer experiments using multiple-pulse sequences or shaped pulses and for moving from model systems to real applications in disordered systems.

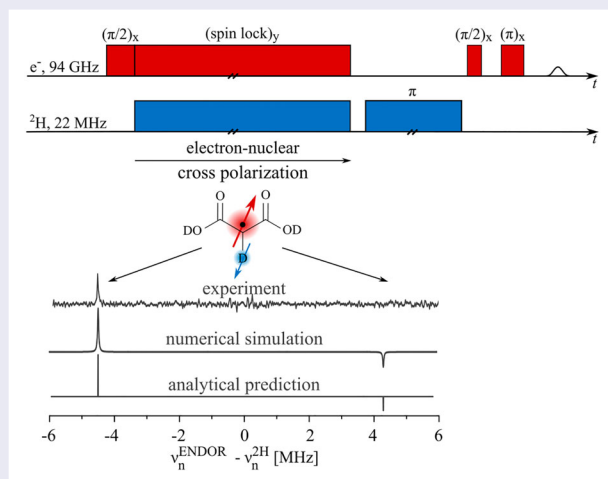
ARTICLE HISTORY



Received 22 February 2020



Accepted 23 April 2020

KEYWORDS

ENDOR; EPR; cross polarisation; spin polarisation; NMR



CONTACT Steffen J. Glaser  glaser@tum.de  Department of Chemistry, Technical University of Munich, Lichtenbergstr 4, Garching 85747, Germany; Munich Center for Quantum Science and Technology (MCQST), Schellingstrasse 4, München 80799, Germany;

Marina Bennati  marina.bennati@mpibpc.mpg.de  Research Group EPR Spectroscopy, Max Planck Institute for Biophysical Chemistry, Am Fassberg 11, Göttingen 37077, Germany Department of Chemistry, Georg-August-Universität Göttingen, Tammannstr. 2, Göttingen 37077, Germany

[†]Current address: Department of Chemistry, Technical University of Munich, Lichtenbergstr 4, 85747 Garching, Germany

1. Introduction

Polarisation transfer between electron and nuclear spins provides the basis of several fundamental spectroscopic experiments. The amount of transferable spin polarisation depends on the relative size of the electron and nuclear gyromagnetic ratios, which is 658:1 and 4286:1 for proton (^1H) and deuterium (^2H) nuclear spins, respectively [1–3]. Due to these large factors, polarisation transfer experiments are being exploited in a variety of modern applications. These include, for instance, dynamic nuclear polarisation in NMR and MRI [1], detection of nuclear spins via EPR spectroscopy [2,3], ODMR detection of nuclear spins with NV centres [4], and coherent control of spin states for solid-state quantum technologies [5]. Nevertheless, a theoretical description in conjunction with a quantitative comparison to experiments and the optimisation of pulse schemes still remain challenging. This is a consequence of the complex multilevel nature of the spin system, which usually contains at least one paramagnetic centre coupled to a number of nuclear spins with sizeable and anisotropic hyperfine (hf) interaction and different gyromagnetic ratios. This creates multiple interaction and relaxation pathways.

Electron-nuclear double resonance (ENDOR) is an EPR-based technique that transfers polarisation from electron to nuclear spins to study their hyperfine interactions [6]. Most commonly, the ligand composition and geometry of an experimental spin system are obtained from ENDOR spectroscopy for a variety of applications ranging from material science and quantum information processing to protein investigations [7]. The very first pulsed ENDOR sequences invented by Mims and Davies in the 60's and 70's are nowadays still the most frequently used [8]. In theory, the polarisation can be completely transferred in a two-spin system consisting of an electron and a nuclear spin [9]. However, in practice, due to technical limitations (e.g. pulse imperfections) and the large anisotropy of the hf interaction, only a fraction of this theoretical limit can be achieved. In addition, electron and nuclear spins have very different nutation and relaxation time scales. During an ENDOR pulse sequence, both spin systems are manipulated at the electron timescale, but the electron spin often relaxes much faster than the nuclear spin. Thus, nuclear saturation becomes an additional bottleneck [10]. The relaxation issues are potentially even more crucial for low gamma nuclei, such as ^2H , which are important targets in ENDOR spectroscopy. Several biological ENDOR applications are based on deuterium buffer exchange as, e.g. demonstrated in hydrogen bond studies of photosystem II or *E.coli* RNR [11].

In order to address the sensitivity in ENDOR, we have previously proposed a so-called cross-polarisation edited ENDOR (CP-ENDOR) experiment [12]. The pulse sequence is based on a new polarisation transfer scheme that has emerged from a concept introduced for dynamic nuclear polarisation [13–16]. Specifically, a modified Hartmann-Hahn condition is used to achieve electron-nuclear cross polarisation (eNCP), i.e. to create degeneracy and polarisation transfer between energy states by simultaneous microwave (MW) and radiofrequency (RF) irradiation of the two coupled spins. In analogy to CP in NMR [17,18] and the NOVEL experiment in DNP [19], the electron-spin magnetisation is locked with MW fields irradiated in the direction perpendicular to the external magnetic field. During eNCP, the electron spin can conveniently be described in a frame, in which the quantisation axis is along an effective field that is given by the combination of hf coupling and MW field. The polarisation transfer can be monitored in the so-called eNCP experiment, in which the electron spin echo is detected as a function of the RF and where CP matching conditions are directly observed [14,15]. In contrast, a CP-ENDOR experiment consists of an eNCP sequence at a fixed RF followed by a standard ENDOR read-out sequence to monitor the polarised nuclear transitions. Matching conditions and CP-ENDOR were previously reported for two-spin systems consisting of one electron and one proton both with spin number $\frac{1}{2}$. A theoretical treatment based on the density operator formalism predicted four matching conditions [12,16], which give rise to an asymmetric CP-ENDOR spectrum [12]. These studies also illustrated that CP-ENDOR is more robust against nuclear saturation effects and allows for sequence repetitions on the order of the electron-spin relaxation rate.

The ability to implement complex MW pulses using arbitrary waveform generators (AWG) [20] makes it possible to use sophisticated multiple-pulse sequences and shaped pulses in EPR and DNP experiments [21,22]. In particular, powerful analytical [23] and numerical [16,24] approaches based on optimal control theory can be used to design robust multiple-pulse experiments for optimal performance in the presence of experimental limitations and imperfections. We refer to [21,25] for an overview of the available techniques from optimal control. However, numerical optimizations require a reliable model of the underlying coherent spin dynamics and of relaxation effects. In particular, in applications with vastly different time scales and disorder, a reasonable compromise has to be found between the accuracy and the computational costs of a model. This may make it necessary to use approximations of the spin dynamics and to test experimentally if the errors introduced by these

approximations are small enough to yield reliable predictions of the experimental results. In an effort to develop a general framework to optimise electron-nuclear cross polarisation, we extend here the analysis of CP-ENDOR to spin-1 deuterium nuclei using both an analytical and a numerical approach based on the density operator formalism.

We investigate a single crystal of deuterated malonic acid radical with well-defined EPR and ENDOR transitions. The main differences between the ^1H and ^2H case are the larger size of the multilevel system, the larger difference of their individual Larmor frequencies with respect to the electron Larmor frequency, and the presence of a nuclear quadrupole coupling. The present work describes the eNCP experiment, which originates from the NMR and DNP literature, within a nomenclature and formalism that are consistent with the EPR and ENDOR literature. Particularly, we apply the fictitious spin-1/2 formalism developed for NMR [26] that is rarely used in EPR. Moreover, fast numerical simulation routines are developed that will in the future enable the consideration of arbitrary optimised pulse sequences. Using the spin density operator formalism in conjunction with approximations in regard to spin relaxation, we found a good agreement between the analytical description, numerical simulations, and experimental results.

We summarise the structure of this paper: We start in §2 by describing the eNCP and CP-ENDOR experiments together with the relevant spin system and experimental details. This sets the stage for §3 where the analytical treatment of the CP-ENDOR experiment determines the matching conditions necessary for an eNCP process. We complement the analytical treatment in §3 with numerical simulation techniques in §4 and compare both theoretical results from §3 and §4 with the experiments in §5. We conclude in §6 and various details are deferred to appendices.

2. Description of the experiments and the spin system

2.1. General description

The two experiments analyzed in this article are illustrated in Figure 1. Both pulse sequences consist of an eNCP polarisation transfer step followed by a polarisation read-out sequence. The polarisation transfer is achieved by simultaneous MW and RF irradiation at a specific amplitude and frequency offset (matching conditions), which will be derived in §3. The so-called eNCP experiment (Figure 1(A)) is employed to detect the RF conditions during eNCP, at which the electron

spin is depolarised. Here, the electron spin-lock echo is recorded as a function of the eNCP RF. We note that, except for the detection scheme, this sequence is closely related to the hyperfine decoupling experiment, as described in [27] and [3]. Nevertheless, in hyperfine decoupling ENDOR, a delay between the 90° preparation and the spin-lock pulse plays a key role, differently than in eNCP. In the case of the eNCP experiment, the focus is on the transfer of polarisation between electron and nuclear spins, while in the decoupling experiment the focus is on resolution enhancement and spectrum simplification.

The CP-ENDOR experiment (Figure 1(B)) is performed at a fixed eNCP RF but contains a second RF read-out pulse, which transfers nuclear polarisation back into observable electron polarisation. The detection of the EPR echo as a function of the read-out RF leads to the detection of the polarised nuclear ENDOR transitions. In the following, we will first describe the general features of the spin system involved in these experiments.

We analyze a two-spin system with an electron spin $\frac{1}{2}$ ($S = \frac{1}{2}$) and a nuclear spin 1 ($I = 1$). We define ω_e and ω_n as the Larmor frequencies of the electron (e) and the nuclear (n) spin, respectively. The spin quantum numbers $m_s = \pm\frac{1}{2}$ for $S = \frac{1}{2}$ are written as $\alpha_e = +\frac{1}{2}$, $\beta_e = -\frac{1}{2}$, where the subscripts denote the electron. The spin quantum numbers $m_I = 0, \pm 1$ for $I = 1$ are written as $\alpha_n = +1$, $\beta_n = 0$, $\gamma_n = -1$, where the subscripts denote the nucleus. The spin Hamiltonian is given in the laboratory frame H_0^{lab} and using the high-field approximation (only z components of spin operators are used) by [28]

$$H_0^{\text{lab}} = \mu_B g_e S_z B_0 - \mu_N g_n I_z B_0 + \hbar A S_z I_z + \hbar \omega_Q \left(\frac{3}{2} I_z^2 - 1 \right). \quad (1a)$$

The first two terms are the electron and nuclear Zeeman interactions with the electron and nuclear magnetons μ_B and μ_N , respectively. The third term is the hf interaction and the fourth term is the nuclear quadrupolar interaction for a spin 1. The electron g factor is considered isotropic and the gyromagnetic ratio of deuterium is positive, i.e. $g_n \mu_N / \hbar > 0$. In angular frequency units with $\omega_e = 2\pi \nu_e = 2\pi \nu_{\text{EPR}}$ and $\omega_n = 2\pi \nu_n = \omega_n^{2\text{H}} = 2\pi \nu_n^{2\text{H}}$, one obtains

$$\mathcal{H}_0^{\text{lab}} = \frac{H_0^{\text{lab}}}{\hbar} = \omega_e S_z + \omega_n I_z + A S_z I_z + \omega_Q \left(\frac{3}{2} I_z^2 - 1 \right). \quad (1b)$$

We explicitly neglect the anisotropy of hf interaction (usually expressed through an additional term $B S_z I_x$ [3]) as this is not required for the discussed eNCP process, in contrast to the general NMR CP case [18]. An explicit consideration of this anisotropy

would considerably complicate the analytical description. Within this approximation, the quadrupole term is axially symmetric with $\hbar\omega_Q = \frac{1}{2}e^2qQ$ (for $I = 1$), where Q is the scalar quadrupole moment and $e \cdot q$ is the zz component of the field gradient at the nucleus. Here, $\mathbb{1}$ denotes a 6×6 unit matrix. The matrix representations of the operators S_z and I_z are tabulated in Appendix 1. The Hamiltonian (1) gives rise to six energy levels with three allowed EPR transitions ($|\Delta m_s| = 1$, $\Delta m_I = 0$), as represented in Figure 1(C). These transitions are denoted by EPR α , EPR β , and EPR γ , as they are associated to the nuclear spin states α_n , β_n , and γ_n , respectively. We note that the sign of the hf coupling A inverts the direction of the hf shift in the electron spin manifolds. For a positive A (Figure 1(D)), the EPR γ_n transition occurs at a lower angular frequency than the α_n transition, and vice versa for a negative A (Figure 1(F)). Most importantly, the spin states from $|1\rangle$ to $|6\rangle$ are sorted according to decreasing

energies, corresponding to the $m_s m_I$ wave functions displayed in Figure 1(C). This order, which is unchanged for $A < 0$, will substantially simplify the description in §4, but requires that a suitable basis change is applied to the spin Hamiltonian (§3, Appendix 2).

The ENDOR lines arise from the allowed nuclear transitions with $|\Delta m_I| = 1$, $\Delta m_S = 0$ (Figure 1(C)). As the ENDOR detection occurs after a selective EPR excitation, only ENDOR transitions that share one common energy level with the excited EPR transition are detected. Specifically, the excitation on the EPR γ transition [1–4] in Figure 1(C) results in only the two observable ENDOR transitions [1–2] and [4–5]. Similarly, the excitation of EPR α [3–6] gives rise to the two ENDOR transitions [5–6] and [2–3]. However, the excitation of EPR β [2–5] gives rise to the four ENDOR lines [1–2], [2–3], [4–5], and [5–6] (Figure 1(E)). All these ENDOR lines will be discussed in §3 and §5.

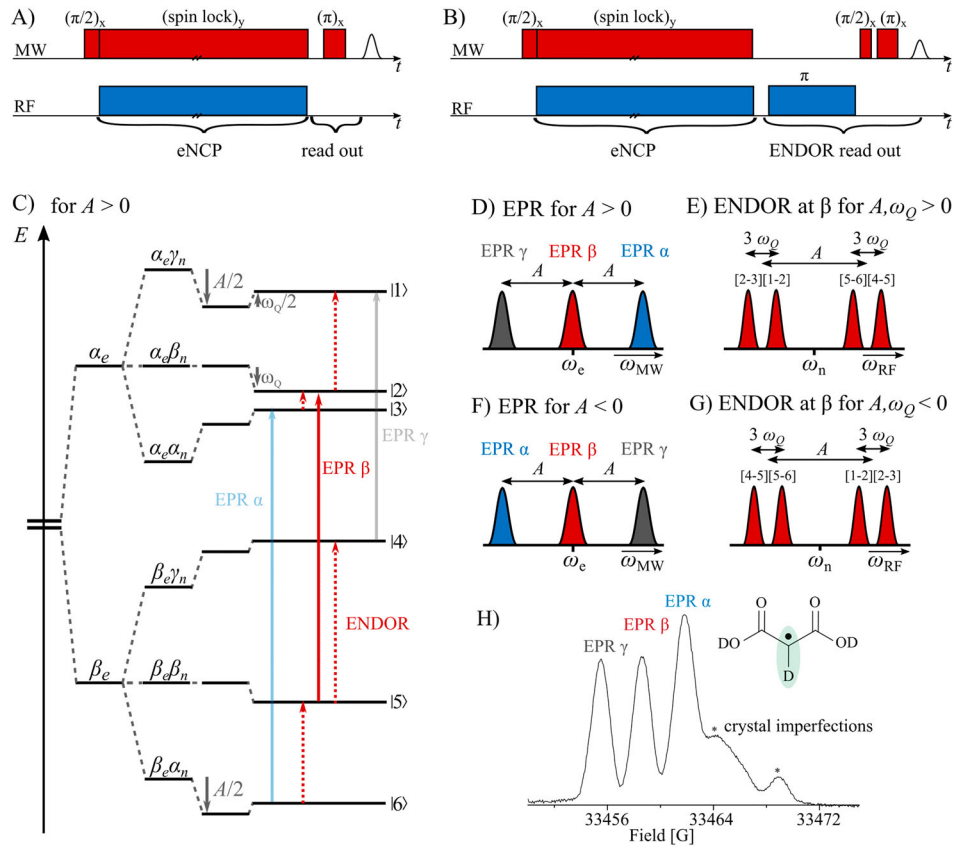


Figure 1. (A, B) Schemes of the eNCP (A) and CP-ENDOR (B) experiments investigated in this work. The two RF pulses in (B) are not phase-locked and chosen as $+x$ pulses, see §2.3. (C) First-order energy diagram for $S = 1/2$, $I = 1$, and hf coupling $A > 0$. The ordering of energy levels corresponds to the Hamiltonian $\tilde{\mathcal{H}}$ in the tilde basis as defined in Appendix 2 (see also §3). (D) Illustration of EPR resonances for $A > 0$. (E) Illustration of the ENDOR lines for the excitation of EPR β for $A > 0$. The shape of the spectrum represents the standard Davies ENDOR experiment. (F) Illustration of the EPR resonances for $A < 0$, malonic acid case. (G) Illustration of the ENDOR transitions for the excitation of EPR β and $A, \omega_Q < 0$, malonic acid case. (H) 94 GHz echo-detected ESE spectrum of a malonic-acid single crystal ($S = 1/2$, $I = 1$). The ESE spectrum ($t_{\pi/2} - \tau - t_{\pi}$ echo) was recorded with $t_{\pi/2} = 20$ ns and $\tau = 500$ ns using one scan at $T = 40$ K. Inset: chemical structure of the perdeuterated malonic acid radical.

2.2. Experimental details

Experiments were performed on a commercial Bruker Elexsys E680 EPR spectrometer operating at $\nu_{\text{EPR}} = 94$ GHz (W-band). A commercial Bruker ENDOR probe head (Bruker TeraFlex) fed with an RF power of about 200 Watt (Amplifier Research) delivered a deuterium RF inversion pulse of $t_{\pi, \text{rf}} \approx 25 \mu\text{s}$, as measured by nuclear-Rabi nutation experiments. All spectra are centred at the deuterium Larmor frequency of $\nu_n^{2\text{H}} \cong 22$ MHz at an external magnetic field of 3.4 Tesla. All experiments were performed at a temperature of $T \approx 40$ K. Detailed experimental parameters are given in the corresponding figure captions.

The experiments were performed with a single crystal of perdeuterated malonic acid radicals (ETH Zürich). The samples were treated by γ -irradiation from a ^{60}Co source and are stable in air. A small crystal was sliced to a height of 0.2 cm and inserted into a quartz sample tube with inner (ID) and outer (OD) diameter of 0.5 and 0.9 mm (Wilmad). The capillary was sealed at both ends. After the sample tube was inserted into the magnet, a particular crystal orientation was determined for which the hyperfine coupling A approximately agrees with the isotropic value a_{iso} . The sample tube was rotated until the desired orientation was identified and the resulting EPR spectrum was recorded. This results in a deuterium hf and quadrupole coupling of $A/2\pi \approx -8.9$ MHz and $\omega_Q/2\pi = -0.04$ MHz, respectively. In this case, the high-field condition in equation (1) approximately holds because $\omega_n > A$ (while assuming $B \approx 0$ at this orientation).

In the single crystal of the perdeuterated malonic acid, the molecule contains an unpaired electron spin that is strongly coupled to one single deuteron (^2H) at the methylene position (Figure 1(H) inset, green). The small couplings of the deuterons at the carboxyl groups are not considered in this study and can be neglected. The echo-detected EPR spectrum of the malonic-acid single crystal is displayed in Figure 1(H) and shows three resolved hf lines with an orientation-dependent hf splitting. The hf couplings to the carboxyl-group deuterons are not resolved but contribute to a visible line broadening. We note that the spectrum is recorded as a function of the magnetic field and not of the MW frequency, therefore the assignment of the three hf lines is interchanged as compared to Figure 1(F).

2.3. Specifying the eNCP and CP-ENDOR pulse sequences

To specify the eNCP and CP-ENDOR pulse sequences and the corresponding MW and RF irradiation with

frequencies ω_{MW} and ω_{RF} , we first introduce the spin Hamiltonian

$$\mathcal{H}_0 = \Delta\omega_e S_z + \Delta\omega_n I_z + AS_z I_z + \omega_Q (3I_z^2 - \mathbb{1}) \quad (2)$$

in the electron-nuclear doubly rotating frame [14] with $\Delta\omega_e = \omega_e - \omega_{\text{MW}}$ and $\Delta\omega_n = \omega_n - \omega_{\text{RF}}$. Recall that the MW and RF amplitudes are given by $\omega_{1e} = \frac{g_e \mu_B B_{1e}}{\hbar}$ and $\omega_{1n} = -\frac{g_n \mu_N B_{1n}}{\hbar}$. The MW amplitude ω_{1e} could be in principle varied in the different steps of the pulse sequence, but it was kept constant for all MW irradiations in the experiments. Note that $|\omega_{1e}| \gg |\omega_{1n}|$ (MHz vs kHz) in contrast to the standard CP case in NMR [18]. Moreover, we have now used definitions consistent with the EPR literature [3]. According to the definition, the sign in front of the nuclear offset term is here positive, in contrast to our previous paper [12]. However, note that both, nuclear Larmor ω_n and ω_{RF} are negative, which must be taken into account in the calculation of §3. A negative RF arises from the circularly polarised component of the linearly polarised RF field in the rotating wave approximation, which has the same rotation direction as the nuclear Larmor frequency.

We now discuss the pulse sequences starting with the eNCP case which is illustrated in Figure 1(A). The experiment was performed with MW excitation and detection on resonance with one EPR transition (i.e. $\Delta\omega_e = \pm A/2\pi$ or $\Delta\omega_e = 0$ MHz). Two orthogonal MW channels with the same MW amplitude were employed. The pulse sequence starts with a selective $\pi/2$ pulse, here set of the duration $t_{\pi/2} \approx 200$ ns, on the x channel and the power on both channels was attenuated accordingly. In this first time period, the Hamiltonian is given by $\mathcal{H}_0 + \omega_{1e} S_x$. The excitation pulse is followed by simultaneously irradiated MW and RF pulses (Figure 1(A)). In order to keep the duty cycle below 1% (which avoids heating effects), the maximal duration was set to an approximate value of $150 \mu\text{s}$. This length is a compromise between eNCP population transfer rates ($\sim \omega_{1n}$), T_2 relaxation and the mentioned heating effects. The phase of the MW pulse was set on the y channel. The concomitant RF pulse uses a RF that is stochastically set for each frequency point of the spectrum. This second period can be modelled by the Hamiltonian $\mathcal{H}_0 + \omega_{1e} S_y + \omega_{1n} I_x$. The third time period is a free evolution of an approximate duration of $1 \mu\text{s}$ with the Hamiltonian \mathcal{H}_0 . The fourth time period is a selective MW-detection π pulse of duration $t_\pi \approx 400$ ns, the corresponding Hamiltonian is $\mathcal{H}_0 + \omega_{1e} S_x$. Before the detection, the fifth time period is a free evolution with an approx. duration of $1 \mu\text{s}$ to refocus the electron spin magnetisation.

We now discuss the pulse sequence for CP-ENDOR (Figure 1(B)). The MW part is similar to the eNCP experiment. The RF part employs two frequency channels that do not need to be phase-locked as the phase of the ENDOR inversion pulse is irrelevant. The pulse sequence starts again with a selective preparation $\pi/2$ pulse of 200 ns duration on the x channel. As in eNCP, the second time period consists of a spin-lock MW pulse concomitant with an RF pulse, which is set at a fixed RF denoted by $\omega_{\text{RF}}^{\text{CP}}$ and an approximate duration of 150 μs . Relative to this, the offset of the nuclear Larmor frequency is $\Delta\omega_n^{\text{CP}} = \omega_n - \omega_{\text{RF}}^{\text{CP}}$. The corresponding Hamiltonian is given by $\mathcal{H}_0 + \omega_{1e}S_y + \omega_{1n}I_x$. The third time period is a short delay, with a free evolution of approximate 1 μs and the Hamiltonian \mathcal{H}_0 . The fourth time period is an ENDOR read-out π pulse with an approximate duration of 30 μs . The frequency $\omega_{\text{RF}}^{\text{ENDOR}}$ of this pulse was stochastically varied over the ENDOR frequency range using one acquisition shot per RF (1 shot/point). The corresponding Hamiltonian is given by $\mathcal{H}_0 + \omega_{1n}I_x$. It follows a short delay, with a free evolution of approx. duration of 1 μs . Afterwards, a MW spin-echo detection sequence of the form $t_{\pi/2} - \tau - t_{\pi}$ is applied, which consists again of a selective $\pi/2$ pulse of duration $t_{\pi/2} \approx 200$ ns on the x channel, a free evolution of approx. duration of 1 μs , and a selective π pulse of $t_{\pi} \approx 400$ ns on the x channel. Before the detection, there is another free evolution of duration 1 μs to refocus the echo. Using this MW sequence, practically no EPR echo is observed without an ENDOR effect. The ENDOR effect results in a non-zero, positive echo. Note, that the induced ENDOR echo is significantly smaller than the primary electron-spin echo as the former results only from spin packets contributing to an ENDOR effect.

3. Theoretical treatment of the CP-ENDOR experiment

3.1. eNCP matching conditions for a two-spin system with $S = 1/2$ and $I = 1$

To describe the spin system under the effect of MW and RF irradiation during eNCP (Figure 1(A and B)), we employ the density operator formalism introduced previously [12,14,29]. The evolution of the density operator $\rho(t)$ under the effect of a time-dependent Hamiltonian $\mathcal{H}(t)$ can be analyzed using the Liouville-von Neumann equation $\dot{\rho}(t) = -i[\mathcal{H}(t), \rho(t)]$ and its formal solution $\rho(t) = U(t)\rho(0)U^{-1}(t)$ [30]. The first part of the following theoretical treatment aims at finding the relevant Hamiltonian for eNCP and subsequently the so-called matching conditions for the polarisation transfer. The matching conditions describe the conditions for which

energy eigenstates become degenerate under simultaneous MW and RF irradiation. This derivation requires the following three steps: (i) specify the spin Hamiltonian (1) under the effect of MW and RF and transform it in a time-independent form, i.e. in a doubly rotating frame. This will allow us to rewrite the formal solution as $\rho(t) = e^{-i\mathcal{H}t}\rho(0)e^{i\mathcal{H}t}$, with $U = \exp(-i\mathcal{H}t)$; (ii) diagonalise the eNCP Hamiltonian (which we denote as the transformation into a so-called *tilted* frame) in the limit of weak RF irradiation; (iii) find the MW and RF irradiation conditions in this *tilted* frame for which pairs of states become degenerate and which drives the corresponding polarisation transfer. Subsequently, the effect of the eNCP Hamiltonian on $\rho(t)$ will be evaluated in Sect. 3.2.

As CP-ENDOR deals with population transfers between energy levels, its analysis keeps track of individual states. Hence it is convenient to convert (1) into the basis $\tilde{\mathcal{H}}$, in which the elements are numbered according to the energy scheme of Figure 1(C) (from high to low energy). The corresponding basis transformation $\tilde{\mathcal{H}} = P\mathcal{H}P$ is given in Appendix 2, where $P = P^{-1}$. In this new representation, EPR transitions α_n , β_n , and γ_n occur between the states [3–6], [2–5], and [1–4], as shown in Figure 1(C). We note that the same basis transformation has to be applied also to all spin operators (Appendix 2). To analyze $\tilde{\mathcal{H}}$ under MW and RF irradiation, we rewrite it in the electron-nuclear doubly rotating frame [14] as in equation (2)

$$\begin{aligned} \tilde{\mathcal{H}} = & \Delta\omega_e\tilde{S}_z + \Delta\omega_n\tilde{I}_z + A\tilde{S}_z\tilde{I}_z + \omega_Q(3\tilde{I}_z^2 - 1) \\ & + \omega_{1e}\tilde{S}_y + \omega_{1n}\tilde{I}_x. \end{aligned} \quad (3a)$$

Equation (3a) is conveniently reformulated using the fictitious spin- $1/2$ operators according to their definitions in Appendix 3 [26]. To simplify the notation, the tilde on the single transition operators is omitted:

$$\begin{aligned} \tilde{\mathcal{H}} = & (\Delta\omega_e - A)I_z^{1-4} + \Delta\omega_e I_z^{2-5} + (\Delta\omega_e + A)I_z^{3-6} \\ & + \omega_{1e}(I_y^{1-4} + I_y^{2-5} + I_y^{3-6}) \\ & + \omega_Q(I_z^{1-2} - I_z^{2-3} + I_z^{4-5} - I_z^{5-6}) \\ & - 2\Delta\omega_n(I_z^{1-2} + I_z^{2-3} + I_z^{4-5} + I_z^{5-6}) \\ & + \omega_{1n}\sqrt{2}(I_x^{1-2} + I_x^{2-3} + I_x^{4-5} + I_x^{5-6}) \end{aligned} \quad (3b)$$

From the above expression, we note that the electronic part of the Hamiltonian (first four terms of equation (3b)) comprises three manifolds ([1–4], [2–5], [3–6]) that can be diagonalised independently from each other, leaving the nuclear part (last three terms) aside. Diagonalization is performed via three consecutive unitary transformations $U\tilde{\mathcal{H}}U^{-1}$ with $U(\theta_\gamma, \theta_\beta, \theta_\alpha) =$

$U_x^{1-4}(\theta_\gamma)U_x^{2-5}(\theta_\beta)U_x^{3-6}(\theta_\alpha)$ and $U_x(\theta) = e^{-i\theta I_x}$ as illustrated in detail in Appendix 4. In the following, let $\tilde{\mathcal{H}}'$ denote the new *tilted* Hamiltonian. The total transformation does not affect the diagonal part (fifth and sixth term) of the nuclear Hamiltonian (3b), which only shifts the eigenstates of the electronic part of $\tilde{\mathcal{H}}'$. The last term of (3b) is considered as a perturbation. The rotation angles for the individual electronic manifolds are readily obtained as:

$$\begin{aligned}\theta_\gamma &= \tan^{-1}\left(\frac{\omega_{1e}}{\Delta\omega_e - A}\right) & \theta_\beta &= \tan^{-1}\left(\frac{\omega_{1e}}{\Delta\omega_e}\right) \\ \theta_\alpha &= \tan^{-1}\left(\frac{\omega_{1e}}{\Delta\omega_e + A}\right)\end{aligned}\quad (4)$$

Here, $\tan^{-1}(n/d)$ is the four-quadrant inverse tangent operation (implemented e.g. in Matlab by the `atan2(n,d)` function), which takes into account the individual signs of the numerator (n) and denominator (d) of the argument of $\tan^{-1}(n/d)$ to determine the correct quadrant of the resulting angle.

This transformation and the rotation angles are best illustrated by considering the direction of the effective fields in each electronic manifold of (3b). We refer to Figure 2 where the corresponding Pythagoras relations are shown. In the new *tilted* frame, the new z direction coincides for each electronic manifold with the direction of the corresponding effective field. Figure 2 also illustrates that the effective fields of all three manifolds depend on the chosen on-resonance irradiation on either EPR α , β , or γ .

The resulting electronic part of this *tilted* Hamiltonian is given by

$$\begin{aligned}\tilde{\mathcal{H}}'_{\text{electron}} &= \sqrt{(\Delta\omega_e - A)^2 + \omega_{1e}^2} I_z^{1-4} \\ &\quad + \sqrt{\Delta\omega_e^2 + \omega_{1e}^2} I_z^{2-5} \\ &\quad + \sqrt{(\Delta\omega_e + A)^2 + \omega_{1e}^2} I_z^{3-6} \\ &= \omega_\gamma I_z^{1-4} + \omega_\beta I_z^{2-5} + \omega_\alpha I_z^{3-6} \\ \text{with } \omega_\gamma &= \sqrt{(\Delta\omega_e - A)^2 + \omega_{1e}^2}, \\ \omega_\beta &= \sqrt{\Delta\omega_e^2 + \omega_{1e}^2} \text{ and} \\ \omega_\alpha &= \sqrt{(\Delta\omega_e + A)^2 + \omega_{1e}^2}.\end{aligned}\quad (5)$$

The zeroth-order diagonal elements of $\tilde{\mathcal{H}}'$ are subsequently obtained from (3) and (5) as

$$\begin{aligned}E_{|1'\rangle} &= \frac{1}{2}\omega_\gamma - \Delta\omega_n + \frac{1}{2}\omega_Q \\ E_{|2'\rangle} &= \frac{1}{2}\omega_\beta - \omega_Q\end{aligned}$$

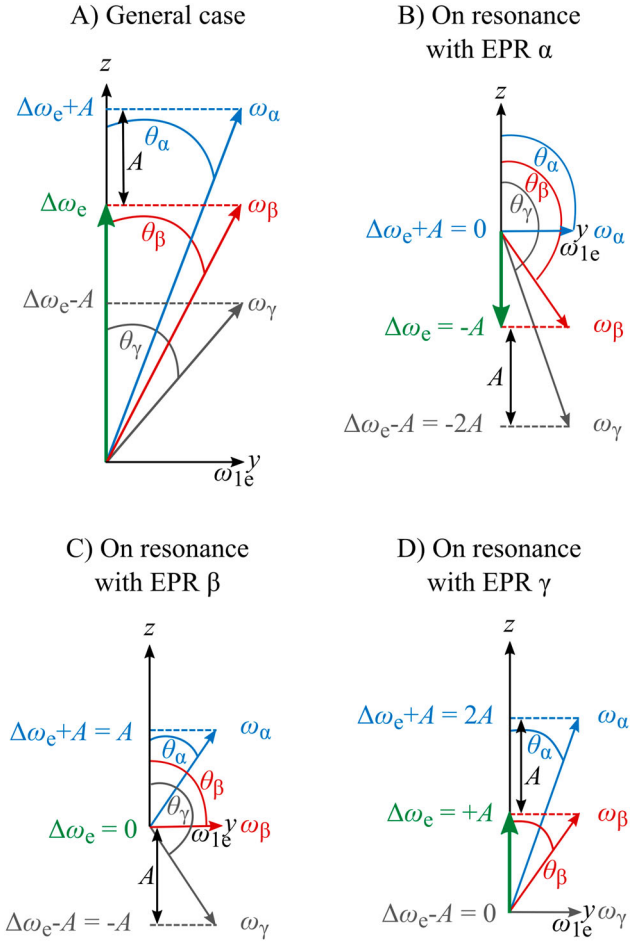


Figure 2. Visualisation of the rotation angles θ_α , θ_β , and θ_γ between the z axis and the effective fields, which are used in the unitary transformation $U(\theta_\gamma, \theta_\beta, \theta_\alpha)$ to obtain equation (5). The general case for $A > 0$ is shown in (A). For $A < 0$ the on-resonance irradiation with the EPR hf line of the α manifold, β manifold, and γ manifold are detailed in (B–D). Axes are labelled in the rotating frame.

$$\begin{aligned}E_{|3'\rangle} &= \frac{1}{2}\omega_\alpha + \Delta\omega_n + \frac{1}{2}\omega_Q \\ E_{|4'\rangle} &= -\frac{1}{2}\omega_\gamma - \Delta\omega_n + \frac{1}{2}\omega_Q \\ E_{|5'\rangle} &= -\frac{1}{2}\omega_\beta - \omega_Q \\ E_{|6'\rangle} &= -\frac{1}{2}\omega_\alpha + \Delta\omega_n + \frac{1}{2}\omega_Q\end{aligned}\quad (6)$$

As indicated by the subscripts, the basis set for the spin states in the new tilted frame is different from the one in the laboratory frame [12]. The remaining off-diagonal terms are proportional to ω_{1n} and can be analytically computed by evaluating the expression $\sqrt{2}\omega_{1n} \cdot U \cdot (I_x^{1-2} + I_x^{2-3} + I_x^{4-5} + I_x^{5-6}) \cdot U^{-1}$. They are negligible unless their magnitude is on the order or larger

than the difference of their interconnecting diagonal elements, which in turn can be tuned by the MW irradiation strength ω_{1e} and the RF irradiation offset $\Delta\omega_n$. This leads to the formulation of CP conditions specifying when pairs of states in the *tilted* frame [$i' - j'$] become degenerate. There also needs to be an off-diagonal element that is the source of the CP process. After numerical inspection of the Hamiltonian matrix after its transformation into the *tilted* frame with $U(\theta_\gamma, \theta_\beta, \theta_\alpha) = U_x^{1-4}(\theta_\gamma)U_x^{2-5}(\theta_\beta)U_x^{3-6}(\theta_\alpha)$, we found that specific pairs of diagonal elements are always connected by off-diagonal elements. By equating the expressions of these pairs from (6) and solving for $\Delta\omega_n$, denoted by $\Delta\omega_n^{\text{CP}}$, we obtain the possible matching conditions

$$\begin{aligned}\Delta\omega_n^{\text{CP}[1'-5']} &= \frac{\omega_\gamma + \omega_\beta + 3\omega_Q}{2} \\ \Delta\omega_n^{\text{CP}[2'-6']} &= \frac{+\omega_\beta + \omega_\alpha + 3\omega_Q}{2} \\ \Delta\omega_n^{\text{CP}[1'-2']} &= \frac{+\omega_\gamma - \omega_\beta + 3\omega_Q}{2} \\ \Delta\omega_n^{\text{CP}[5'-6']} &= \frac{-\omega_\beta + \omega_\alpha + 3\omega_Q}{2} \\ \Delta\omega_n^{\text{CP}[4'-5']} &= \frac{-\omega_\gamma + \omega_\beta + 3\omega_Q}{2} \\ \Delta\omega_n^{\text{CP}[2'-3']} &= \frac{+\omega_\beta - \omega_\alpha + 3\omega_Q}{2} \\ \Delta\omega_n^{\text{CP}[2'-4']} &= \frac{-\omega_\gamma - \omega_\beta + 3\omega_Q}{2} \\ \Delta\omega_n^{\text{CP}[3'-5']} &= \frac{-\omega_\beta - \omega_\alpha + 3\omega_Q}{2}\end{aligned}\quad (7)$$

Rotation angles and matching conditions were calculated for hf and quadrupole parameters of the malonic acid single crystal used in the experiment (Tables 1 and 2). In the crystal orientation selected for this study, the hf coupling constant of -8.9 MHz is close to the isotropic value of ≈ -9 MHz (from the tensor values $A_x/2\pi = -4.4$ MHz, $A_y/2\pi = -8.9$ MHz, and $A_z/2\pi = -14$ MHz) and the quadrupole coupling value is $\omega_Q/2\pi = -0.04$ MHz (from the tensor with $\omega_{Q,x}/2\pi = 0.07$ MHz, $\omega_{Q,y}/2\pi = -0.03$ MHz, and $\omega_{Q,z}/2\pi = -0.04$ MHz) [31]. The MW field strength was $\omega_{1e}/2\pi = 1.25$ MHz. From equation 4 and for the considered case of $|A| \gg \omega_{1e}$, $A < 0$, we obtain the set of

Table 1. Rotation angles for the perdeuterated malonic acid ($|A| \gg \omega_{1e}$, $A < 0$) when the MW excitation is resonant either with EPR α , β , or γ respectively.

	EPR α [3-6]	EPR β [2-5]	EPR γ [1-4]
θ_α	$\pi/2$	π	π
θ_β	0	$\pi/2$	π
θ_γ	0	0	$\pi/2$

Table 2. Calculated matching conditions for deuterated malonic acid parameters $A/2\pi = -8.9$ MHz, $\omega_Q/2\pi = -0.04$ MHz, and $\omega_{1e}/2\pi = 1.25$ MHz.

	EPR α [3-6] $\Delta\omega_e = -A/2\pi$	EPR β [2-5] $\Delta\omega_e = 0$	EPR γ [1-4] $\Delta\omega_e = A/2\pi$
Degenerated states	$\Delta\omega_n^{\text{CP}}/2\pi$ [MHz]	$\Delta\omega_n^{\text{CP}}/2\pi$ [MHz]	$\Delta\omega_n^{\text{CP}}/2\pi$ [MHz]
[1'-2']	-4.4	+3.9	+3.9
[1'-5']	-13.4	-5.1	-5.1
[2'-3']	-3.8	+3.9	+4.5
[2'-4']	+13.5	+5.2	+5.2
[2'-6']	-5.1	+5.2	-13.4
[3'-5']	+5.2	-5.1	+13.5
[4'-5']	+4.5	-3.8	-3.8
[5'-6']	+3.9	-3.8	-4.4

MW offsets $\Delta\omega_e = \omega_e - \omega_{\text{MW}}$ for the individual EPR lines are also illustrated in Figure 1(F). For instance, $\Delta\omega_e$ results in a positive sign for EPR α due to the negative sign of the hf coupling. The calculation considers that the nuclear Larmor frequency ω_n and $\omega_{\text{RF}}^{\text{CP}}$ in $\Delta\omega_n^{\text{CP}}$ (equation 7) are negative. The highlighted matching conditions are efficient only if associated to the respective EPR line (see text).

angles given in Table 1. The polarisation transfer and the CP-ENDOR effect can occur if a matching condition is fulfilled. A matching condition is realised by setting the RF irradiation during MW spin lock at one of the expected (equation 7) $\Delta\omega_n^{\text{CP}}$ offsets. However, there are two additional requirements: (i) there must be a non-negligible probability for polarisation transfer (see above) and (ii) the populations of the matched states must lead to a population re-distribution. This latter point will be illustrated in §3.2. From a numerical inspection of the tilted frame Hamiltonian using the malonic acid parameters, we find that some matching conditions in Table 2 are only weakly allowed, specifically the ones at ± 13 MHz, as compared to all others. In §3.2 we will analyse whether the remaining conditions will lead to an observable ENDOR effect. The results are anticipated here, i.e. these matching conditions are highlighted in Table 2 and are referred to as ‘CP-efficient’.

3.2. CP-ENDOR intensities

We use the density operator formalism introduced in Sect. 3.1 to predict the intensities of the CP-ENDOR lines. By selecting a suitable rotating frame and neglecting relaxation, the pulse sequence can be generally subdivided into a finite number of time segments with a time-independent Hamiltonian, and this evolution might be examined analytically using the product operator formalism for an electron coupled to one nuclear spin [9]. Due to the complexity of the CP-sequence, which involves a long spin-lock pulse in which T_2 relaxation is non-negligible, as well as two RF pulses with distinct frequencies, this approach is not feasible. However, it was previously illustrated [12] that a simpler description of

the eNCP effect on the elements of ρ can be derived from a heuristic treatment for both the eNCP RF irradiation as well as the spin relaxation. This is justified by the fact that the spin-lock pulse is long enough for coherences to decay during the pulse. Thus, at the end of the spin lock, the electron spin can be considered to be aligned along the direction of its effective field (see Figure 2). To examine this process, we express ρ during eNCP in the eigenbasis of the tilted Hamiltonian. This is achieved by transforming the eNCP propagator into the tilted frame [12] ($e^{-i\tilde{\mathcal{H}}t} \rightarrow e^{-i\tilde{\mathcal{H}}'t}$) with the help of the unitary matrix U ($U^{-1}U = 1$) as $e^{-i\tilde{\mathcal{H}}t} = U^{-1}Ue^{-i\tilde{\mathcal{H}}t}U^{-1}U = U^{-1}e^{-i(U\tilde{\mathcal{H}}U^{-1})t}U = U^{-1}e^{-i\tilde{\mathcal{H}}'t}U$ with U , $\tilde{\mathcal{H}}$, and $\tilde{\mathcal{H}}'$ as given in §3.1. The rotation direction used to diagonalise $\tilde{\mathcal{H}}$ is important and explained in Appendix 4. We insert this transformation into the computation of the density matrix during eNCP, (t_{CP}), and obtain

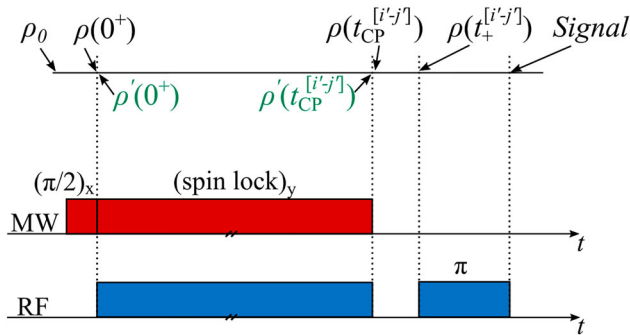
$$\begin{aligned}\rho(t_{CP}) &= e^{-i\tilde{\mathcal{H}}t_{CP}}\rho(0^+)e^{i\tilde{\mathcal{H}}t_{CP}} \\ &= U^{-1} \cdot \{e^{-i\tilde{\mathcal{H}}'t_{CP}} \cdot (U\rho(0^+)U^{-1}) \cdot e^{+i\tilde{\mathcal{H}}'t_{CP}}\} \cdot U\end{aligned}\quad (8)$$

where $\rho(0^+)$ and $\rho(t_{CP})$ are the density matrices in the doubly rotating frame at the beginning and the end of the eNCP process, respectively (Scheme 1). The expression in the curly brackets represents the time evolution of the density matrix $\rho'(t_{CP})$ in the tilted frame (Scheme 1). In the following, we illustrate this procedure for the spin system with $S = 1/2$, $I = 1$.

The density operator at thermal equilibrium is given in the high-temperature approximation by

$$\rho_B = \frac{\mathbb{1} - \beta\hbar\tilde{\mathcal{H}}}{\text{Tr}\{\mathbb{1}\}} \quad (9)$$

with $\beta = 1/k_B T$. (Note: We prefer here the more general symbol ρ for the density matrix [2,32] instead of the



Scheme 1. Definitions of the density operators at the analyzed steps of the pulse sequence. The primed superscript together with the green colour refers to the tilted frame as compared to the rotating frame.

reduced spin density matrix σ [3,30] for consistency with the magnetic resonance literature [12,14,16]). Here, we have $\text{Tr}\{\mathbb{1}\} = 6$ for the case of a spin system with $S = 1/2$ and $I = 1$. It follows that

$$\rho_B = \frac{\mathbb{1}}{6} - \frac{1}{6}\beta\hbar\tilde{\mathcal{H}}. \quad (10)$$

The traceless part

$$\rho_0 = -\frac{1}{6}\frac{\hbar\gamma_e B_0}{k_B T}\tilde{S}_Z = -R\tilde{S}_Z \quad (11)$$

is relevant for the computation of the expectation values of the spin operators and we set $R = \frac{1}{6}\frac{\hbar\gamma_e B_0}{k_B T}$. Using a compact notation for diagonal matrices with the diagonal elements as introduced in Appendix 2, we have

$$\rho_0 = -R\tilde{S}_Z = -R \begin{bmatrix} 1/2 & & & \\ & 1/2 & & \\ & & 1/2 & \\ & & & -1/2 \\ & & & -1/2 & \\ & & & & -1/2 \end{bmatrix}, \quad (12)$$

where the expectation value of \tilde{S}_Z is given by $\tilde{S}_Z = \hbar\text{Tr}\{\rho_0\tilde{S}_Z\} = -1.5R\hbar$. In the following, we transform the relevant elements of the density matrix according to the steps in Scheme 1.

The first step in the CP sequence is a selective preparation ($\pi/2$)_x pulse on one of the three EPR transitions (as $|A| \gg \omega_{1e}$). At the beginning of the sequence, the density matrix is denoted by $\rho(0) = \rho_0$. If the MW excitation acts, for instance, selectively on the EPR α transition [3–6], the density matrix $\rho(0^+)$ is after the preparation pulse in Scheme 1 equal to

$$\begin{aligned}\rho(0^+) &= e^{-i\frac{\pi}{2}I_x^{3-6}}\{-R\tilde{S}_Z\}e^{i\frac{\pi}{2}I_x^{3-6}} \\ &= e^{-i\frac{\pi}{2}I_x^{3-6}}\{-R(I_z^{1-4} + I_z^{2-5} + I_z^{3-6})\}e^{i\frac{\pi}{2}I_x^{3-6}} \\ &= -R(I_z^{1-4} + I_z^{2-5} - I_y^{3-6}).\end{aligned}\quad (13)$$

Here, we have substituted \tilde{S}_Z with single-transition operators (see Appendix 3) and used the rotation properties of spin operators (see Appendix 5). In the next step of the sequence (i.e. during the MW spin lock), the component I_y^{3-6} is locked with the on-resonant MW irradiation along y . We now transform $\rho(0^+)$ into the tilted frame of the EPR α manifold according to equation 8 with $\rho'(0^+) = U\rho(0^+)U^{-1}$ and $U = U_x(\theta_\gamma, \theta_\beta, \theta_\alpha)$ as given in Appendix 4. Considering Table 1 for malonic acid, the angles for the transformation are $\theta_\alpha = \frac{\pi}{2}$, $\theta_\beta = 0$, and $\theta_\gamma = 0$. We obtain (Scheme 1)

$$\rho'(0^+) = e^{-i\theta_\gamma I_x^{1-4}} e^{-i\theta_\beta I_x^{2-5}} e^{-i\theta_\alpha I_x^{3-6}}$$

$$\begin{aligned}
& \times \{-R(I_z^{1-4} + I_z^{2-5} - I_y^{3-6})\}e^{+i\theta_y I_x^{1-4}} \\
& \times e^{+i\theta_\beta I_x^{2-5}} e^{+i\theta_\alpha I_x^{3-6}} \\
& = e^{-i\frac{\pi}{2} I_x^{3-6}} \{-R(I_z^{1-4} + I_z^{2-5} - I_y^{3-6})\}e^{+i\frac{\pi}{2} I_x^{3-6}} \\
& = -RI_z^{1-4} - RI_z^{2-5} + RI_z^{3-6}. \quad (14)
\end{aligned}$$

Now, we can heuristically examine the effect of the CP RF pulse on equation (14). When no CP condition is matched or no RF field is applied during the spin lock, the diagonal elements of ρ' stay locked and decay with the characteristic relaxation time $T_{1\rho}$. Other density-matrix elements will decay with a shorter time $T_{2\rho}$ and due to dephasing by the inhomogeneities in ω_{1e} . We note that this step alone leads to an ENDOR effect as it creates a magnetisation profile of \tilde{S}_Z as a function of $\Delta\omega_e$ after the spin-lock pulse [33]. If the RF irradiation is applied during the spin-lock period with one matching condition met, population is transferred between matched states. In the presence of relaxation, this will have the net effect of equalising populations among the matched states at the end of the long spin-lock pulse [12]. For example, starting from equation (14), the matching conditions $[i' - j']$ at EPR α (see Table 2) result in $\rho'(t_{CP}^{[i' - j']})$ (Scheme 1):

$$\begin{aligned}
\rho'(0^+) &= \begin{bmatrix} -R/2 \\ -R/2 \\ R/2 \\ R/2 \\ R/2 \\ -R/2 \end{bmatrix} \rightarrow \rho'(t_{CP}^{[2' - 3']}) \\
&= \begin{bmatrix} -R/2 \\ -R/2 + R/2 \\ \frac{2}{+R/2 - R/2} \\ R/2 \\ R/2 \\ -R/2 \end{bmatrix} = \begin{bmatrix} -R/2 \\ 0 \\ 0 \\ R/2 \\ R/2 \\ -R/2 \end{bmatrix} \quad (15) \\
\rho'(0^+) &= \begin{bmatrix} -R/2 \\ -R/2 \\ R/2 \\ R/2 \\ R/2 \\ -R/2 \end{bmatrix} \rightarrow \rho'(t_{CP}^{[5' - 6']}) \\
&= \begin{bmatrix} -R/2 \\ -R/2 \\ R/2 \\ R/2 \\ \frac{2}{+R/2 - R/2} \\ -R/2 + R/2 \end{bmatrix} = \begin{bmatrix} -R/2 \\ -R/2 \\ R/2 \\ R/2 \\ 0 \\ 0 \end{bmatrix}
\end{aligned}$$

In contrast, the density-matrix elements remain unchanged if a degeneracy is created between the levels $1'$ and $2'$, i.e.

$$\begin{aligned}
\rho'(0^+) &= \begin{bmatrix} -R/2 \\ -R/2 \\ R/2 \\ R/2 \\ R/2 \\ -R/2 \end{bmatrix} \rightarrow \rho'(t_{CP}^{[1' - 2']}) \\
&= \begin{bmatrix} -R/2 - R/2 \\ \frac{2}{-R/2 - R/2} \\ R/2 \\ R/2 \\ R/2 \\ -R/2 \end{bmatrix} = \begin{bmatrix} -R/2 \\ -R/2 \\ R/2 \\ R/2 \\ R/2 \\ -R/2 \end{bmatrix}. \quad (16)
\end{aligned}$$

Next, the density matrix after the eNCP step is transferred back into the doubly rotating frame via the inverse transformation $\rho(t_{CP}) = U^{-1}\rho'(t_{CP}^{[i' - j']})U$, according to equation (8). We note that while $\rho'(t_{CP})$ is diagonal (i.e. the magnetisation aligns along the effective field), $\rho(t_{CP})$ in the doubly rotating frame is not diagonal. However, after the spin-lock pulse, the spin system evolves freely for a time $\tau > T_{2e}$ and now also the off-diagonal elements of $\rho(t_{CP})$ decay and can be neglected for the detection scheme. Accordingly, the density matrix $\rho(t_+^{[i' - j']})$ (Scheme 1) after eNCP and prior to the ENDOR RF pulse is obtained from equation (15) as

$$\begin{aligned}
\rho(t_+^{[2' - 3']}) &= \begin{bmatrix} -R/2 \\ 0 \\ -R/4 \\ R/2 \\ R/2 \\ -R/4 \end{bmatrix}, \\
\rho(t_+^{[5' - 6']}) &= \begin{bmatrix} -R/2 \\ -R/2 \\ R/4 \\ R/2 \\ 0 \\ R/4 \end{bmatrix}. \quad (17)
\end{aligned}$$

We can now calculate the ENDOR effect after a selective RF π pulse on one of the allowed ENDOR transitions connected to the transition EPR α (see Figure 1(b) and §2). The ENDOR signal for the selective detection on EPR α is proportional to the expectation value of I_z^{3-6} . For instance, for an RF inversion on the nuclear transition $[5-6]$ after CP $[2' - 3']$ we get:

Table 3. Calculated signal intensities of CP-ENDOR for $S = 1/2$, $I = 1$ and parameters from Tables 1 and 2 for malonic acid and excitation/detection on the given EPR lines.

	EPR α [3–6]		EPR β [2–5]			EPR γ [1–4]		
	ENDOR [2–3]	ENDOR [5–6]	ENDOR [1–2]	ENDOR [2–3]	ENDOR [4–5]	ENDOR [5–6]	ENDOR [1–2]	ENDOR [4–5]
CP [1'–2']	$-\frac{2}{8}R$	$-\frac{2}{8}R$	$-\frac{3}{8}R$	$-\frac{3}{8}R$	$\frac{1}{8}R$	$-\frac{1}{8}R$	$-\frac{2}{8}R$	$-\frac{2}{8}R$
CP [1'–5']	$-\frac{2}{8}R$	$-\frac{2}{8}R$	$-\frac{2}{8}R$	$-\frac{2}{8}R$	$-\frac{2}{8}R$	$-\frac{2}{8}R$	$\frac{1}{8}R$	$-\frac{3}{8}R$
CP [2'–3']	$\frac{1}{8}R$	$-\frac{3}{8}R$	$-\frac{2}{8}R$	$-\frac{2}{8}R$	$-\frac{2}{8}R$	$-\frac{2}{8}R$	$-\frac{2}{8}R$	$-\frac{2}{8}R$
CP [2'–4']	$-\frac{2}{8}R$	$-\frac{2}{8}R$	$-\frac{2}{8}R$	$-\frac{2}{8}R$	$-\frac{2}{8}R$	$-\frac{2}{8}R$	$-\frac{3}{8}R$	$\frac{1}{8}R$
CP [2'–6']	$-\frac{2}{8}R$	$-\frac{2}{8}R$	$-\frac{3}{8}R$	$-\frac{3}{8}R$	$-\frac{1}{8}R$	$\frac{1}{8}R$	$-\frac{2}{8}R$	$-\frac{2}{8}R$
CP [3'–5']	$-\frac{2}{8}R$	$-\frac{2}{8}R$	$-\frac{1}{8}R$	$\frac{1}{8}R$	$-\frac{3}{8}R$	$-\frac{3}{8}R$	$-\frac{2}{8}R$	$-\frac{2}{8}R$
CP [4'–5']	$-\frac{2}{8}R$	$-\frac{2}{8}R$	$\frac{1}{8}R$	$-\frac{1}{8}R$	$-\frac{3}{8}R$	$-\frac{3}{8}R$	$-\frac{2}{8}R$	$-\frac{2}{8}R$
CP [5'–6']	$-\frac{3}{8}R$	$\frac{1}{8}R$	$-\frac{2}{8}R$	$-\frac{2}{8}R$	$-\frac{2}{8}R$	$-\frac{2}{8}R$	$-\frac{2}{8}R$	$-\frac{2}{8}R$

$$\begin{aligned}
 \text{Signal}^{\text{EPR}\alpha}(\text{RF56, CP23}) \\
 &\sim \text{Tr}\{(U_{\pi}^{5-6}) \cdot \rho(t_+^{[2'-3']}) \cdot (U_{\pi}^{5-6})^{-1} \cdot I_z^{3-6}\} \\
 &\sim \text{Tr}\{\rho(t_+^{[2'-3']}) \cdot (U_{\pi}^{5-6})^{-1} \cdot I_z^{3-6} \cdot (U_{\pi}^{5-6})\} \\
 &\sim \text{Tr}\{\rho(t_+^{[2'-3']}) \cdot I_z^{3-5}\} = -3/8R \quad (18)
 \end{aligned}$$

The first line of equation 18 is identical to the second line of equation 18 because the operators under the trace can be cyclically permuted. The ENDOR intensities were calculated analogously for all matching conditions of Table 2. The matching conditions at EPR α that result in efficient polarisation transfer are highlighted in Table 2. The calculation was also performed for a selective excitation of EPR β and EPR γ as detailed in Appendix 6. All these results are summarised in Table 3.

The calculation predicts that the polarisation transfer should deliver an antiphase ENDOR spectrum with absolute intensity ratios 1:3, in analogy to the results for a two-spin system with $S = 1/2$ and $I = 1/2$. If, however, no matching condition is active, the calculation predicts a symmetric ENDOR effect (so-called spin-lock ENDOR effect). Interestingly, for an active CP-ENDOR, quadrupolar coupling doublets in the central (EPR β) manifold are predicted with an additional antiphase structure.

4. Numerical density-matrix simulation of a quantum system consisting of one electron spin $1/2$ and one nuclear spin 1

4.1. Recalling the eNCP and CP-ENDOR sequence

We start by adding pulses (controls) for S_x , S_y , I_x , and I_y to the spin Hamiltonian \mathcal{H}_0 from equation (2) in electron-nuclear doubly rotating frame. This leads to

$$\begin{aligned}
 \mathcal{H}(t) &= \mathcal{H}_0 + 2\pi[u_x(t)S_x + u_y(t)S_y + v_x(t)I_x + v_y(t)I_y] \\
 &= \Delta\omega_e S_z + \Delta\omega_n I_z + AS_z I_z + \omega_Q(\frac{3}{2}I_z^2 - \mathbb{1}) \quad (19)
 \end{aligned}$$

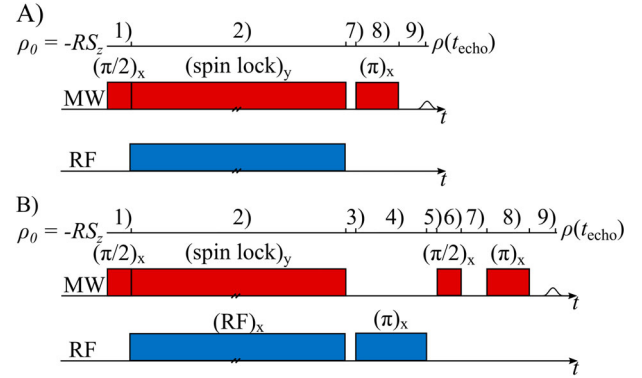


Figure 3. eNCP (A) and CP-ENDOR (B) simulation steps. The initial state for all simulations is $\rho_0 = -RS_z$ which evolves to $\rho(t_{\text{echo}})$ at the time of the echo. Five steps are considered in the eNCP simulation and nine steps in CP-ENDOR.

Note: The numbering of the steps was adapted to represent both sequences.

$$+ 2\pi[u_x(t)S_x + u_y(t)S_y + v_x(t)I_x + v_y(t)I_y]. \quad (20)$$

The pulse amplitudes (control functions) $u_x(t)$, $u_y(t)$, $v_x(t)$, and $v_y(t)$ detail how the Hamiltonian changes during the time evolution. For the numerical simulation discussed in this section, we again set ω_{MW} on resonance with one EPR transition (i.e. $\Delta\omega_e = \pm A/2\pi$ or $\Delta\omega_e = 0$ MHz) but $\Delta\omega_n$ is set to $\Delta\omega_n = \Delta\omega_n^{\text{CP}} = \omega_n - \omega_{\text{RF}}^{\text{CP}}$ for the whole pulse sequence (but see §4.4 for a more efficient simulation of the ENDOR step). This is in contrast to the discussion in §2.3 and allows us to numerically compute the time evolution in a single and fixed rotating frame. We point out that the numerical simulation uses the standard basis of the spin Hamiltonian. To compute the time evolution of the density matrix, we build on the discussion in §2.3 and subdivide the eNCP and CP-ENDOR sequences into consecutive steps, as defined in Figure 3.

Both sequences start from the (traceless deviation) density matrix $\rho_0 = -RS_z$. The eNCP and CP-ENDOR

sequence consists of five and nine steps, respectively. We focus here on the CP-ENDOR sequence as its steps are similar to the respective steps of the eNCP sequence (Figure 3). The CP-ENDOR sequence is repeated at a fixed CP frequency $\Delta\omega_n^{\text{CP}}$ while varying the so-called ENDOR frequency $\Delta\omega_n^{\text{ENDOR}} = \omega_n - \omega_{\text{RF}}^{\text{ENDOR}}$. The corresponding Hamiltonians are

$$1) \mathcal{H}_1 := \mathcal{H}_0 + \omega_{1e}S_x \quad (21)$$

$$2) \mathcal{H}_2 := \mathcal{H}_{\text{CP}} := \mathcal{H}_0 + \omega_{1e}S_y + \omega_{1n}I_x \quad (22)$$

$$3) \mathcal{H}_3 := \mathcal{H}_0 \quad (23)$$

$$4) \mathcal{H}_4(t) := \mathcal{H}_{\text{ENDOR}}(t) \\ := \mathcal{H}_0 + \omega_{1n} \cos(\Delta\omega_{\text{RF}}^{\text{Diff}} t) I_x \\ + \omega_{1n} \sin(\Delta\omega_{\text{RF}}^{\text{Diff}} t) I_y \quad (24)$$

$$5) \mathcal{H}_5 := \mathcal{H}_3 := \mathcal{H}_0 \quad (25)$$

$$6) \mathcal{H}_6 := \mathcal{H}_1 := \mathcal{H}_0 + \omega_{1e}S_x \quad (26)$$

$$7) \mathcal{H}_7 := \mathcal{H}_0 \quad (27)$$

$$8) \mathcal{H}_8 := \mathcal{H}_0 + \omega_{1e}S_x \quad (28)$$

$$9) \mathcal{H}_9 := \mathcal{H}_7 := \mathcal{H}_0 \quad (29)$$

with

$$\Delta\omega_{\text{RF}}^{\text{Diff}} = \omega_{\text{RF}}^{\text{ENDOR}} - \omega_{\text{RF}}^{\text{CP}}.$$

As stated in §2, the two RF channels in the experiment corresponding to $\omega_{\text{RF}}^{\text{CP}}$ and $\omega_{\text{RF}}^{\text{ENDOR}}$ do not need to be phase locked as the phase of the ENDOR inversion pulse is irrelevant. In the simulation, we arbitrarily choose the phase of the ENDOR pulse to be x, see Figures 1 and 3.

Similar to §2.3, equations (21) to (29) describe the time evolution in the various steps of the CP-ENDOR pulse sequence shown in Figure 3. It starts with a selective $\pi/2$ pulse on the electron spin along the +x direction in equation (21) and continues with the eNCP step where constant irradiation is applied to the electron spin along the +y direction and to the nuclear spin along the +x direction. Recall from above that $\Delta\omega_n$ in \mathcal{H}_0 is set to the eNCP frequency $\Delta\omega_n^{\text{CP}}$. It follows a free evolution [equation (23)] and the ENDOR step which applies a modulated irradiation $\mathcal{H}_4(t) = \mathcal{H}_{\text{ENDOR}}(t)$ on the nuclear spin, where $\Delta\omega_{\text{RF}}^{\text{Diff}}$ specifies the ENDOR frequency $\omega_{\text{RF}}^{\text{ENDOR}}$ relative to the eNCP frequency $\omega_{\text{RF}}^{\text{CP}}$. Equations (25) to (29) detail free evolutions and selective irradiations on the electron spin. Recall from §2.3 that the pulse durations are $t_1 = 200$ ns, $t_2 = 150$ μ s, $t_3 = t_5 = t_7 = t_9 \approx 1$ μ s, $t_4 \approx 30$ μ s, $t_6 = 200$ ns, $t_8 = 400$ ns.

4.2. General numerical simulation strategy

Our general simulation strategy critically relies on the doubly rotating frame that we have chosen to model our experimental setup. The chosen rotating frame allows us to treat almost all Hamiltonians \mathcal{H}_j that act during the time steps of the CP-ENDOR sequence as time independent. Only the Hamiltonian $\mathcal{H}_4(t) = \mathcal{H}_{\text{ENDOR}}(t)$ for the ENDOR step is not constant. We now describe the general strategy for time-independent Hamiltonians and subsequently discuss the ENDOR step.

Consider a time-independent Hamiltonian \mathcal{H}_j with $j \neq 4$ as specified in Equations (21)–(29). In a time step of duration t_j , the density matrix ρ is mapped to $\rho_j = U_j \cdot \rho_{j-1} \cdot U_j^{-1}$. The unitary matrix $U_j = \exp(-i\mathcal{H}_j t_j)$ is computed by numerical matrix exponentiation. This straightforward strategy is effective as long as the occurring matrices are small enough and this certainly applies to the case of 6×6 matrices used here. In principle, the same strategy could be also applied to the ENDOR step by splitting it into small enough sub-steps, for which one could assume a time-independent Hamiltonian. One would however have to use a very fine resolution to sufficiently capture the modulation. This would lead to a very inefficient approach to numerically simulate the ENDOR step. For example, for a difference frequency $\Delta\omega_{\text{RF}}^{\text{Diff}}/(2\pi) = (\omega_{\text{RF}}^{\text{ENDOR}} - \omega_{\text{RF}}^{\text{CP}})/(2\pi)$ of 10 MHz, one oscillation period corresponds to $T_{\text{osc}} = 1/(\omega_{\text{RF}}^{\text{ENDOR}}/(2\pi)) = 100$ ns. Thus the time steps would need to be smaller than $T_{\text{osc}}/10 = 10$ ns in order to faithfully approach the modulation by a piecewise constant function. For a typical ENDOR period of 30 μ s, this would require at least 3000 time steps to be calculated! A much more efficient approach is detailed in the following Section 4.3.

4.3. Efficient simulation of the ENDOR step

In the numerical simulations, the CP-ENDOR sequence is described in a doubly rotating frame. For the nuclear spin I , the rotating frame frequency is chosen to be identical to the RF $\omega_{\text{RF}}^{\text{CP}}$ that is applied during the CP period (step 2). Hence, in this rotating frame, the offset frequency of spin I is given by $\Delta\omega_n^{\text{CP}}$. However, during the ENDOR period (step 4), the irradiated RF $\omega_{\text{RF}}^{\text{ENDOR}}$ is in general different from $\omega_{\text{RF}}^{\text{CP}}$ which results in a time-dependent, oscillating RF Hamiltonian in the rotating frame defined by $\Delta\omega_n^{\text{CP}}$. A computationally efficient approach consists of two simple steps:

- (I) Perform the calculation during the ENDOR period (step 4) in the rotating frame defined by the nuclear

irradiation RF $\omega_{\text{RF}}^{\text{ENDOR}}$, in which the RF Hamiltonian is constant and for which the offset frequency of the nuclear spin is $\Delta\omega_n^{\text{ENDOR}}$ during step 4. Hence the Hamiltonian $\mathcal{H}_4 = \mathcal{H}_{\text{ENDOR}}(t)$ given in the CP rotating frame in equation (24) corresponding to the RF irradiation at the difference frequency $\Delta\omega_{\text{RF}}^{\text{Diff}} = \omega_{\text{RF}}^{\text{ENDOR}} - \omega_{\text{RF}}^{\text{CP}}$ is translated into the constant term

$$\begin{aligned} \mathcal{H}_{4a} = & \Delta\omega_e S_z + \Delta\omega_n^{\text{ENDOR}} I_z + A S_z I_z \\ & + \omega_Q(3I_z^2 - \mathbb{1}) + \omega_{1n} I_x \end{aligned} \quad (30)$$

and the corresponding propagator is $U_{4a} = \exp(-i\mathcal{H}_{4a}t_4)$.

- (II) In order to take into account the different rotating frame frequency during the ENDOR period of duration t_4 , the density matrix is subsequently transformed by $U_{4b} = \exp(-i\mathcal{H}_{4b}t_4)$ with

$$\mathcal{H}_{4b} = \Delta\omega_{\text{RF}}^{\text{Diff}} I_z. \quad (31)$$

In summary, the density matrix ρ is mapped in the ENDOR step to the density matrix $U_{4b}(U_{4a}\rho U_{4a}^{-1})U_{4b}^{-1}$ using two substeps which can both be modelled using a time-independent Hamiltonian. This provides an efficient approach to compute the coherent effect of the ENDOR step.

4.4. Heuristic simulation of the effect of B_1 inhomogeneity and relaxation

We now discuss how the effect of B_1 inhomogeneity and relaxation was taken into account in our simulations. For example, we could numerically simulate the effect of B_1 inhomogeneity by averaging over repeated numerical simulations for a range of B_1 amplitudes. This would however lead to a significant simulation overhead and a decrease in efficiency. Here, a heuristic approach is used to model the effect of the B_1 inhomogeneity and relaxation accumulated during the second (i.e. CP) and the third step, which are assumed to be the primary incoherent contribution during the CP-ENDOR sequence. After the application of the Hamiltonian $\mathcal{H}_2 = \mathcal{H}_{\text{CP}}$ during the second step, (a) we transform the density matrix into the eigenbasis of $\mathcal{H}_2 = \mathcal{H}_{\text{CP}}$, (b) remove all non-diagonal entries of the density matrix, and (c) transform the density matrix back to its original basis. Physically, it means that we assume complete relaxation/defocusing of magnetisation components transverse to the spin-lock field (or dressed-spin coherence), in other words $T_{2\rho} \ll t_{\text{SL}}$. To simulate the third time step, we apply the unitary U_3 to the density matrix and (d) remove again all of its non-diagonal entries afterwards. We subsequently continue with the fourth step as before. The new substeps (a) to

(c) emulate the averaging effect of the B_1 inhomogeneity and relaxation during the CP step. After the third time step, the substep (d) is supposed to model the effect of fast transverse T_2 relaxation. This heuristic approach leads to only a minor computational overhead while capturing important experimental contributions during the CP-ENDOR sequence.

5. Comparison with the experimental results

Figure 4 illustrates the experimental eNCP spectra recorded with the sequence in Figure 1(A) (experimental settings given in Sec. 2) and their comparison with the analytical predictions (Sec. 3) and the numerical simulations (Sec. 4). Experimental spectra are normalised to the intensity of the spin-lock echo without CP and show peaks at the matching conditions for the depolarisation of the electron spin as a function of the RF offset $\Delta\omega_n^{\text{CP}} = \omega_n - \omega_{\text{RF}}^{\text{CP}}$. For the numerical simulations, the intensities represent the expectation value $-\langle S_y \rangle$, which is produced under the effect of the MW π pulse with $+x$ phase after the spin lock along $+y$. Since the excitation is selective, the probed magnetisation $-\langle S_y \rangle$ (without relaxation and CP) amounts to 1/3 of the initial $\langle S_z \rangle = |1.5R\hbar|$ (Sec 3.2). For the simulation we have employed parameters for malonic acid radical as given in Section 3.1 (see Figure caption). The analytical solutions represent the $\Delta\omega_n^{\text{CP}}/2\pi$ from Table 2 as stick spectra and their intensities are arbitrary.

From Figure 4, we observe eight matching conditions in the region $\Delta\omega_n^{\text{CP}}/2\pi \gtrsim |2|$ MHz arising from the interaction with the strongly coupled deuteron (Figure 1, inset; labelled with D1 in the caption of Figure 4) which satisfy $|A| \gg |\omega_{1e}|$, $A < 0$, and $|A| \gg |\omega_Q|$. The peak positions are in excellent agreement with the analytical predictions from Table 2 and the numerical simulations. Consistent with the theoretical prediction, resonances of matching conditions with low transition probabilities (e.g. at ± 13 MHz) are not detected in the eNCP experiment. The additional peaks around the centre of each eNCP spectrum ($\Delta\omega_n^{\text{CP}}/2\pi = \pm 1.18$ and 0 MHz) are assigned to polarisation transfer to distant, weakly coupled nuclei (labelled with D2 in caption of Figure 4) in analogy to previously published work on a BDPA [14,15] and protonated malonic-acid single crystal [34]. The resonances were numerically simulated with hf and quadrupole parameters $A(D2)/2\pi = -0.1$ MHz, $\omega_Q(D2)/2\pi = 0.0$ MHz.

In the experiment, the intensity of the echo depolarisation is about 10% of the available echo, whereas in the simulation this effect is up to 50% of the observed echo. We suggest that the experimental efficiency is limited by sample imperfections. We observe these

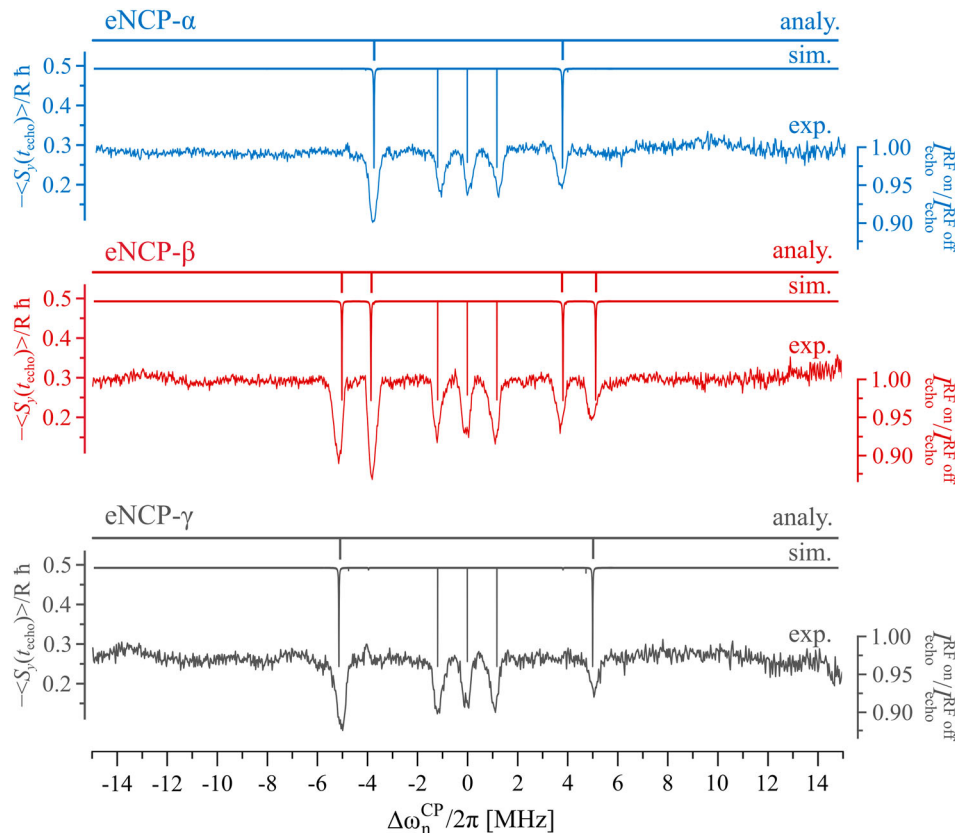


Figure 4. Experimental eNCP spectra recorded selectively on each EPR line (α , β , and γ), transitions according to Table 2 (analy.), and numerical simulations (sim.). Note that the x axis follows the definition $\Delta\omega_n^{\text{CP}} = \omega_n - \omega_{\text{RF}}^{\text{CP}}$. Note also that the different scales of the y axes (left and right) were adapted for a better comparison. *Exp. Conditions:* $\nu_{\text{EPR}} = 94$ GHz, shot repetition time = 100 ms; $t_{\pi/2, \text{mw}} = 200$ ns, $t_{\text{CP}} = 150$ μ s, one shot/point, random RF acquisition, 100–250 scans. *Sim. parameters:* $\omega_{1e}/2\pi = 1.18$ MHz, $\omega_{1n}/2\pi = 10$ kHz, $A(D1)/2\pi = -8.9$ MHz, $A(D2)/2\pi = -0.1$ MHz, $\omega_Q(D1)/2\pi = -0.04$ MHz, $\omega_Q(D2)/2\pi = 0.00$ MHz, $\Delta\omega_e = \pm A/2\pi$, 0 MHz. Line width in the simulated spectra results from power broadening due to the RF pulse.

imperfections in two ways: (1) the EPR spectrum shows additional absorptions (Figure 1) and (2) the three EPR lines shows a line width of about 2 Gauss, which is indicative for some inhomogeneous broadening. It means that there is a little distribution of molecular orientations, which contributes to the CP-ENDOR experiment. These inhomogeneities could lead to spin diffusion after the preparation pulse and echo depolarisation, not considered in the simulations. We believe that additional forthcoming experimental data will help to clarify this point in the future.

Some effect of the parameters ω_{1e} and ω_{1n} on the line shape is illustrated in Appendix 7. While ω_{1e} shifts the position of the matching conditions, as expected, ω_{1n} contributes to its line width. Moreover, in the experiment the intensities at the high-frequency side (negative $\Delta\omega_n^{\text{CP}}$) appear slightly higher. This trend is also observed in the non-matched CP-ENDOR spectrum (e.g. Figure 5(A), top) and in the control Davies-ENDOR experiments (Appendix 8). It is attributed to a deviation from

the high-field approximation, i.e. a so-called hf enhancement [35]. Indeed, an asymmetry of the ENDOR line could be reproduced in a simulation of the Davies-ENDOR spectrum using the software *Easyspin* [36] and complete Hamiltonian diagonalization, Appendix 8. As expected, this asymmetry effect is not seen in our numerical simulations (Figures 4 and 5) which assume high-field conditions.

Subsequently, CP-ENDOR spectra were recorded using the sequence in Figure 1(B) and by setting the RF offset $\Delta\omega_n^{\text{CP}}$ at one of the various detected matching conditions in Figure 4. The spectra and their comparison with theoretical predictions (Table 3) as well as numerical simulations are displayed in Figure 5. We observed two types of ENDOR signals: one for the CP-matched and one for the non CP-matched RF during eNCP. As pointed out in Sec. 3.2, for no ENDOR effect, the electron–spin echo is zero at the detection time, which is reflected in the experiment as well as in the numerical simulation. For the non-matched case, ENDOR signals result in an

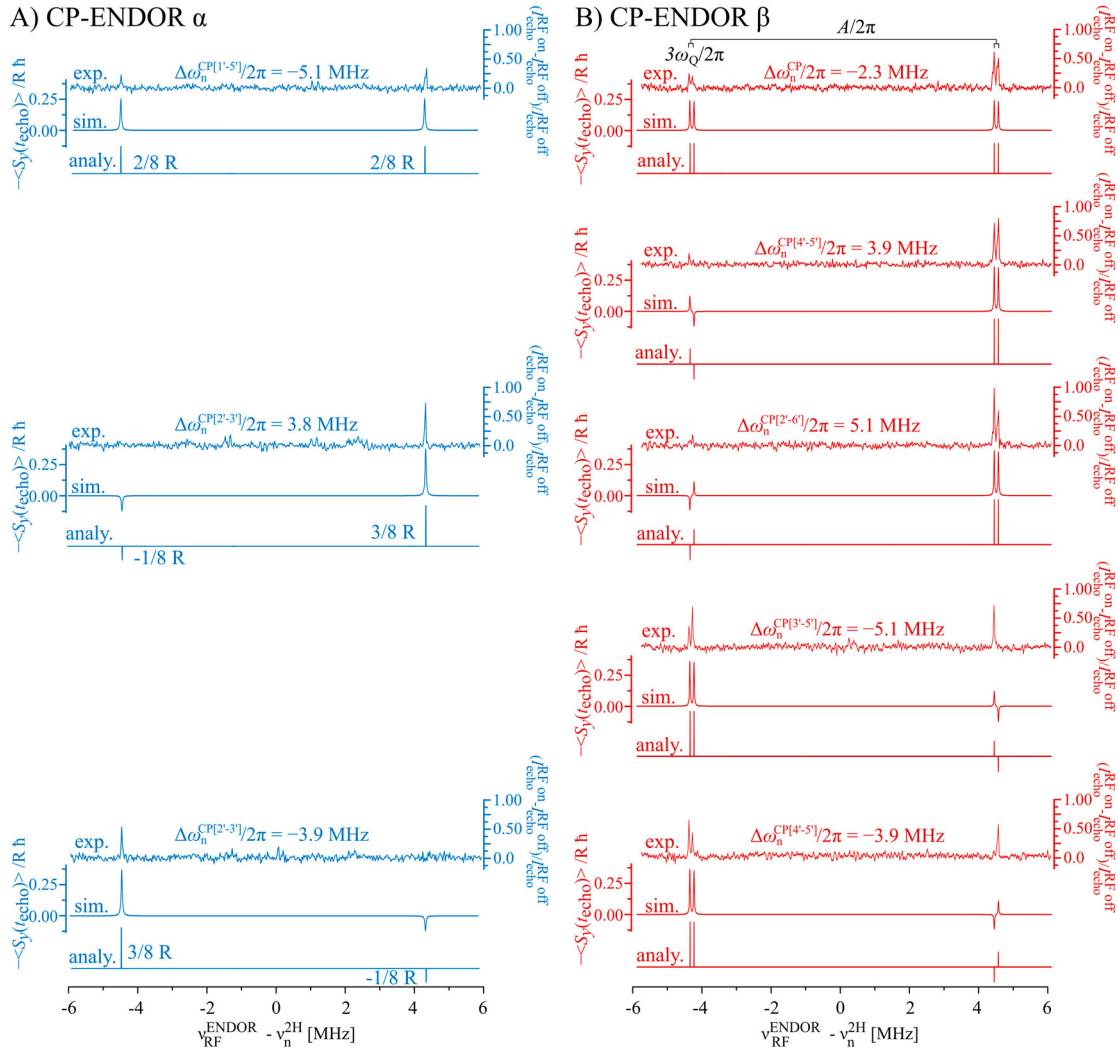


Figure 5. Experimental CP-ENDOR spectra (top lines) on a deuterated malonic-acid single crystal ($S = 1/2, I = 1$), numerical CP-ENDOR simulations (middle lines) and peak intensities according to the analytical prediction in Table 3. Results are shown for the selective excitation of the EPR α in (A) and β in (B), respectively. They are plotted in the ENDOR frequency domain with $\nu_{\text{RF}} = \omega_{\text{RF}}/2\pi$. Experimental RF offsets $\Delta\omega_n^{\text{CP}} = \omega_n - \omega_{\text{RF}}^{\text{CP}}$ according to Figure 4 and their assignments from Table 2 are indicated in each sub-spectrum. *Exp. conditions:* $\nu_{\text{EPR}} = 94 \text{ GHz}$, $t_{\pi/2, \text{mw}} = 200 \text{ ns}$, $t_{\text{CP}} = 150 \text{ }\mu\text{s}$, $t_{\text{ENDOR}} = 25 \text{ }\mu\text{s}$, shot repetition time = 100 ms, 1 shot/point, random RF acquisition, 100 scans each. *Sim. parameters:* $\omega_{1e}/2\pi = 1.18 \text{ MHz}$, $\omega_{1n}/2\pi = 13 \text{ kHz}$, $A/2\pi = -8.9 \text{ MHz}$, $\omega_Q/2\pi = -0.04 \text{ MHz}$, $\Delta\omega_e = \pm A/2\pi$, 0 MHz.

increase of the echo (Figure 5 top) and the lines have a similar intensity, which is consistent with the predictions of Table 3 and the numerical simulations (Figure 5). As in Figure 4, the low-frequency lines appear weaker than the high-frequency lines.

In contrast, the CP-ENDOR intensities for the matched CP RF offset displayed quite different line shapes. Analytical and numerical analysis consistently predicted an antiphase doublet with relative intensities (3:1) (Figure 5(A), Appendix 9 for EPR γ). Similar to the analytical results, the numerically predicted maximal CP-ENDOR effect amounts to $3/4$ of the available magnetisation on one line (left axis). The experiment well reproduced this asymmetry. The weaker negative

line was however not detectable. We assign this effect to sample inhomogeneities, which would readily lead to a cancellation of the negative peaks. For CP-ENDOR with a detection on EPR β (Figure 5(B)), the analytical and numerical techniques consistently predicted four lines (Figure 1(E)) with one antiphase doublet of lower intensity. Experimentally, this pattern was also observed but only the absorptive line of the antiphase doublet was visible. Again, we suggest that the absence of the negative peak is due to a cancellation resulting from sample inhomogeneities, which are not considered in the analytical treatment, as we neglect any off-resonance effects. Recent analysis of powder patterns [33,37] indicated that negative peaks disappear in the presence of

such inhomogeneities. Nevertheless, the overall agreement between different theoretical predictions and the experimental data is striking and not obvious, as the analytical prediction of intensities (Table 3) does not explicitly calculate a time evolution of the density operator during the spin lock, whereas the numerical simulation does. This underlines the validity of our model for the effective description of this experiment.

Finally, it is interesting to compare the results with a standard Davies ENDOR experiment. The observed theoretical and experimental Davies ENDOR intensities are stronger than the CP effect (Figure A2), i.e. the echo change amounts to approx. $\langle \tilde{S}_z \rangle / 3$. This means that in principle, Davies ENDOR delivers the most efficient ENDOR effect, at least in this single crystal case. However, in the case of disordered systems and for slow nuclear relaxation, CP-ENDOR might be an attractive alternative [37].

6. Conclusion

We have theoretically and experimentally demonstrated CP-ENDOR on a ^2H nuclear spin, which is an important target in structural studies of biological systems and materials. In particular, we have used a single crystal of deuterated malonic acid to experimentally identify the matching conditions for cross-polarisation between an electron $S = 1/2$ and a nuclear spin $I = 1$ under consideration of a small quadrupolar interaction ($|Q| \ll |A|$). Probing the resulting ENDOR intensities after the eNCP transfer resulted in asymmetric spectra with intensity trends similar to that reported in ^1H studies. The predicted and simulated matching conditions agreed well with the experiment. The line shape of the CP-ENDOR spectra was reasonably consistent with the theoretical prediction of an ideal two-spin system. Therefore, the presented analytical investigation and the simulation strategy provide a framework to expand studies to more advanced polarisation transfer schemes, using for instance optimised pulses and to analyze results in disordered, powder-like systems as in frozen protein solutions.

Acknowledgements

IB and MB would like to thank Prof. Gunnar Jeschke (Laboratory of physical Chemistry, ETH Zürich) for donating the single crystal of perdeuterated malonic acid radical.

Disclosure statement

No potential conflict of interest was reported by the author(s).

Funding

This work was supported by the DFG Priority Program 1601. R.Z. and S.J.G. acknowledge support from the Deutsche Forschungsgemeinschaft (DFG, German Research Foundation) through grant number Gl 203/7-2. S.J.G. acknowledges funding by the Deutsche Forschungsgemeinschaft (DFG, German Research Foundation) under Germany's Excellence Strategy 390814868 (EXC-2111). R.Z. acknowledges funding from the European Union's Horizon 2020 research and innovation programme under grant agreement number 817482 (PASQuanS).

References

- [1] V.K. Michaelis, R.G. Griffin, B. Corzilius, and S. Vega, *Handbook of High Field Dynamic Nuclear Polarization* (Wiley, Chichester, 2020).
- [2] M. Mehring and V.A. Weberruss, *Object-oriented Magnetic Resonance* (Academic Press, London, 2001).
- [3] A. Schweiger and G. Jeschke, *Principles of Pulse Electron Paramagnetic Resonance* (Oxford University Press, Oxford, 2001).
- [4] P. Fernandez-Acebal, O. Rosolio, J. Scheuer, C. Muller, S. Muller, S. Schmitt, L.P. McGuinness, I. Schwarz, Q. Chen, A. Retzker, B. Naydenov, F. Jelezko, and M.B. Plenio, *Nano. Lett.* **18** (3), 1882 (2018); F. Shagieva, S. Zaiser, P. Neumann, D.B.R. Dasari, R. Stöhr, A. Denisenko, R. Reuter, C.A. Meriles, and J. Wrachtrup, *Nano. Lett.* **18** (6), 3731 (2018); M.H. Abobeih, J. Randall, C. E. Bradley, H. P. Bartling, M. A. Bakker, M. J. Degen, M. Markham, D. J. Twitchen, and T.H. Taminiau, *Nature* **576** (2019).
- [5] P. London, J. Scheuer, J.M. Cai, I. Schwarz, A. Retzker, M.B. Plenio, M. Katagiri, T. Teraji, S. Koizumi, J. Isoya, R. Fischer, L.P. McGuinness, B. Naydenov, and F. Jelezko, *Phys. Rev. Lett.* **111** (6), 067601 (2013); S. Simmons, R.M. Brown, H. Riemann, N.V. Abrosimov, P. Becker, H.J. Pohl, M.L. Thewalt, K.M. Itoh, and J.J. Morton, *Nature* **470** (7332), 69 (2011); T. Uden, N. Tomek, T. Weggler, F. Frank, P. London, J. Zopes, C. Degen, N. Raatz, J. Meijer, H. Watanabe, K.M. Itoh, M.B. Plenio, B. Naydenov, and F. Jelezko, *npj Quantum Information* **4** (1) (2018); I. Schwartz, J. Scheuer, B. Tratzmiller, S. Müller, Q. Chen, I. Dhand, Z. Wang, C. Müller, B. Naydenov, F. Jelezko, and M.B. Plenio, *Sci. Adv.* **4** (8), eaat8978 (2018).
- [6] J.R. Harmer, in *EPR Spectroscopy: Fundamentals and Methods*, edited by D. Goldfarb, S. Stoll (Wiley, Chichester, 2018), pp. 331–357.
- [7] T. Argirevic, C. Riplinger, J. Stubbe, F. Neese, and M. Bennati, *J. Am. Chem. Soc.* **134**, 17661 (2012); D. Goldfarb, *PCCP* **8** (20), 2325 (2006); S. Zaiser, T. Rendler, I. Jakobi, T. Wolf, S. Lee, S. Wagner, V. Bergholm, T. Schulte-Herbrüggen, P. Neumann, and J. Wrachtrup, *Nat. Comm.* **7**, 12279 (2016).
- [8] W.B. Mims, *Proc. Roy. Soc. Lond. Ser. A.* **283** (1395), 452 (1965); E.R. Davies, *Phys. Lett. A* **47** (1), 1 (1974).
- [9] C. Gemperle and A. Schweiger, *Chem. Rev.* **91**, 1481 (1991).
- [10] A.M. Tyryshkin, J.J.L. Morton, A. Ardavan, and S.A. Lyon, *J. Chem. Phys.* **124**, 234508 (2006); J.J.L. Morton, N.S. Lees, B.M. Hoffman, and S. Stoll, *J. Magn. Reson.* **191** (2),

- 315 (2008); B. Epel, A. Pöpl, P. Manikandan, S. Vega, and D. Goldfarb, *J. Magn. Reson.* **148**, 388 (2001).
- [11] S. Keßen, C. Teutloff, J. Kern, A. Zouni, and R. Bittl, *ChemPhysChem.* **11** (6), 1275 (2010); T.U. Nick, K.R. Ravichandran, J. Stubbe, M. Kasanmascheff, and M. Bennati, *Biochemistry* **56** (28), 3647 (2017).
- [12] R. Rizzato, I. Kaminker, S. Vega and M. Bennati, *Mol. Phys.* **111** (18–19), 2809 (2013).
- [13] S.R. Hartmann and E.L. Hahn, *Phys. Rev.* **128** (5), 2042 (1962).
- [14] V. Weis, M. Bennati, M. Rosay, and R.G. Griffin, *J. Chem. Phys.* **113** (16), 6795 (2000).
- [15] V. Weis and R.G. Griffin, *Sol. State Nuc. Magn. Reson.* **29** (1), 66 (2006).
- [16] N. Pomplun, B. Heitmann, N. Khaneja, and S.J. Glaser, *Appl. Magn. Reson.* **34**, 331 (2008).
- [17] A. Pines, M.G. Gibby, and J.S. Waugh, *J. Chem. Phys.* **59** (2), 569 (1973).
- [18] L. Müller and R.R. Ernst, *Mol. Phys.* **38** (3), 963 (1979).
- [19] K.O. Tan, S. Jawla, R.J. Temkin, and R.G. Griffin, *eMagRes* **8** (3), 339–352 (2019).
- [20] P.E. Spindler, Y. Zhang, B. Endeward, N. Gershernzon, T.E. Skinner, S.J. Glaser, and T.F. Prisner, *J. Magn. Reson.* **218**, 49 (2012); T. Kaufmann, T.J. Keller, J.M. Franck, R.P. Barnes, S.J. Glaser, J.M. Martinis, and S. Han, *J. Magn. Reson.* **235**, 95 (2013).
- [21] P.E. Spindler, P. Schöps, W. Kallies, S.J. Glaser, and T.F. Prisner, *J. Magn. Reson.* **280**, 30 (2017).
- [22] A. Doll and G. Jeschke, *J. Magn. Reson.* **280**, 46 (2017).
- [23] N. Khaneja, R. Brockett, and S.J. Glaser, *Phys. Rev. A.* **63** (3), 032308 (2001); N. Khaneja, T. Reiss, B. Luy, and S.J. Glaser, *J. Magn. Reson.* **162** (2), 311 (2003); N. Khaneja, J.-S. Li, C. Kehlet, B. Luy, and S. J. Glaser, *Proc. Nat. Acad. Sci. USA* **101** (41), 14742 (2004); N. Khaneja, F. Kramer, and S. J. Glaser, *J. Magn. Reson.* **173** (1), 116 (2005); R. Zeier, H. Yuan, and N. Khaneja, *Phys. Rev. A* **77**(3), 032332 (2008).
- [24] N. Khaneja, T. Reiss, C. Kehlet, T. Schulte-Herbrüggen and J. Glaser, *J. Magn. Reson.* **172** (2), 296 (2005); T.E. Skinner, T.O. Reiss, B. Luy, N. Khaneja, and S.J. Glaser, *J. Magn. Reson.* **167** (1), 68 (2004); N. Pomplun and S.J. Glaser, *PCCP* **12** (22), 5791 (2010); H. Yuan, R. Zeier, N. Pomplun, S.J. Glaser, and N. Khaneja, *Phys. Rev. A* **92** (5), 053414 (2015).
- [25] S.J. Glaser, U. Boschain, T. Calarco, C.P. Koch, W. Köckenberger, R. Kosloff, I. Kuprov, B. Luy, S. Schirmer, T. Schulte-Herbrüggen, D. Sugny and F.K. Wilhelm, *Eur. Phys. J. D* **69** (12), 279 (2015).
- [26] S. Vega, *J. Chem. Phys.* **68** (12), 5518 (1978).
- [27] G. Jeschke and A. Schweiger, *J. Chem. Phys.* **106** (24), 9979 (1997).
- [28] C.P. Poole and H.A. Farach, *Theory of Magnetic Resonance* (Wiley, New York, 1987).
- [29] G. Jeschke and A. Schweiger, *Mol. Phys.* **88**, 355 (1996).
- [30] A. Feintuch and S. Vega, in *eMagRes* **6** (4), 427–452 (2017).
- [31] A. Sanderud, E. Sagstuen, Y. Itagaki and A. Lund, *J. Phys. Chem. A* **104** (27), 6372 (2000).
- [32] M.H. Levitt, *Spin Dynamics, Basic of Nuclear Magnetic Resonance* (Wiley, Chichester, 2001).
- [33] I. Bejenke, PhD Thesis, University of Göttingen (2019).
- [34] R. Rizzato and M. Bennati, *PCCP* **16** (17), 7681 (2014).
- [35] L.R. Dalton and A.L. Kwiram, *J. Chem. Phys.* **57** (3), 1132 (1972).
- [36] S. Stoll and A. Schweiger, *J. Magn. Reson.* **178** (1), 42 (2006).
- [37] R. Rizzato and M. Bennati, *Chem. Phys. Chem.* **16** (18), 3769 (2015).
- [38] J.J. Sakurai, *Modern Quantum Mechanics* (Addison-Wesley Publishing Company Inc., New York, 1985).

Appendices

Appendix 1. Spin-operator definitions

We consider a quantum system that consists of one electron spin $S = 1/2$ and one nuclear spin $I = 1$. The corresponding density-matrix description relies on the generalised Pauli matrices

$$\sigma_x^S := \frac{1}{2} \begin{bmatrix} 0 & 1 \\ 1 & 0 \end{bmatrix}, \sigma_y^S := \frac{1}{2} \begin{bmatrix} 0 & -i \\ i & 0 \end{bmatrix},$$

$$\sigma_z^S := \frac{1}{2} \begin{bmatrix} 1 & 0 \\ 0 & -1 \end{bmatrix}, \mathbb{1}^S := \begin{bmatrix} 1 & 0 \\ 0 & 1 \end{bmatrix}$$

and $\sigma_x^I := \frac{1}{\sqrt{2}} \begin{bmatrix} 0 & 1 & 0 \\ 1 & 0 & 1 \\ 0 & 1 & 0 \end{bmatrix}$, $\sigma_y^I := \frac{1}{\sqrt{2}} \begin{bmatrix} 0 & -i & 0 \\ i & 0 & -i \\ 0 & i & 0 \end{bmatrix}$, $\sigma_z^I := \begin{bmatrix} 1 & 0 & 0 \\ 0 & 0 & 0 \\ 0 & 0 & -1 \end{bmatrix}$, $\mathbb{1}^I := \begin{bmatrix} 1 & 0 & 0 \\ 0 & 1 & 0 \\ 0 & 0 & 1 \end{bmatrix}$ which are used to define the spin operators for the S and I spins:

$$S_x := \sigma_x^S \otimes \mathbb{1}^I = \frac{1}{2} \begin{bmatrix} 0 & 0 & 0 & 1 & 0 & 0 \\ 0 & 0 & 0 & 0 & 1 & 0 \\ 0 & 0 & 0 & 0 & 0 & 1 \\ 1 & 0 & 0 & 0 & 0 & 0 \\ 0 & 1 & 0 & 0 & 0 & 0 \\ 0 & 0 & 1 & 0 & 0 & 0 \end{bmatrix},$$

$$S_y := \sigma_y^S \otimes \mathbb{1}^I = \frac{1}{2} \begin{bmatrix} 0 & 0 & 0 & -i & 0 & 0 \\ 0 & 0 & 0 & 0 & -i & 0 \\ 0 & 0 & 0 & 0 & 0 & -i \\ i & 0 & 0 & 0 & 0 & 0 \\ 0 & i & 0 & 0 & 0 & 0 \\ 0 & 0 & i & 0 & 0 & 0 \end{bmatrix},$$

$$S_z := \sigma_z^S \otimes \mathbb{1}^I = \frac{1}{2} \begin{bmatrix} 1 & 0 & 0 & 0 & 0 & 0 \\ 0 & 1 & 0 & 0 & 0 & 0 \\ 0 & 0 & 1 & 0 & 0 & 0 \\ 0 & 0 & 0 & -1 & 0 & 0 \\ 0 & 0 & 0 & 0 & -1 & 0 \\ 0 & 0 & 0 & 0 & 0 & -1 \end{bmatrix},$$

$$I_x := \mathbb{1}^S \otimes \sigma_x^I = \frac{1}{\sqrt{2}} \begin{bmatrix} 0 & 1 & 0 & 0 & 0 & 0 \\ 1 & 0 & 1 & 0 & 0 & 0 \\ 0 & 1 & 0 & 0 & 0 & 0 \\ 0 & 0 & 0 & 0 & 1 & 0 \\ 0 & 0 & 0 & 1 & 0 & 1 \\ 0 & 0 & 0 & 0 & 1 & 0 \end{bmatrix},$$

$$I_y := \mathbb{1}^S \otimes \sigma_y^I = \frac{1}{\sqrt{2}} \begin{bmatrix} 0 & -i & 0 & 0 & 0 & 0 \\ i & 0 & -i & 0 & 0 & 0 \\ 0 & i & 0 & 0 & 0 & 0 \\ 0 & 0 & 0 & 0 & -i & 0 \\ 0 & 0 & 0 & i & 0 & -i \\ 0 & 0 & 0 & 0 & i & 0 \end{bmatrix},$$

$$I_z := \mathbb{1}^S \otimes \sigma_z^I = \begin{bmatrix} 1 & 0 & 0 & 0 & 0 & 0 \\ 0 & 0 & 0 & 0 & 0 & 0 \\ 0 & 0 & -1 & 0 & 0 & 0 \\ 0 & 0 & 0 & 1 & 0 & 0 \\ 0 & 0 & 0 & 0 & 0 & 0 \\ 0 & 0 & 0 & 0 & 0 & -1 \end{bmatrix}.$$

We also introduce the 6×6 identity matrix $\mathbb{1} := \mathbb{1}^S \otimes \mathbb{1}^I$.

Appendix 2. Transformation of the Hamiltonian into the tilde basis

We will also use a so-called tilde basis for spin operators, which is adapted for a more practical order of the energy levels, where they are numbered from 1 to 6 according to descending energy. The elements in the tilde basis are easily obtained using the transformation $\tilde{M} = PMP$ with

$$P = \begin{bmatrix} 1 & 0 \\ 0 & 1 \end{bmatrix} \otimes \begin{bmatrix} 0 & 0 & 1 \\ 0 & 1 & 0 \\ 1 & 0 & 0 \end{bmatrix} = \begin{bmatrix} 0 & 0 & 1 & 0 & 0 & 0 \\ 0 & 1 & 0 & 0 & 0 & 0 \\ 1 & 0 & 0 & 0 & 0 & 0 \\ 0 & 0 & 0 & 0 & 0 & 1 \\ 0 & 0 & 0 & 0 & 1 & 0 \\ 0 & 0 & 0 & 1 & 0 & 0 \end{bmatrix} = P^{-1}. \quad (\text{A1})$$

This maps the vector basis

$$\begin{bmatrix} \alpha\alpha \\ \alpha\beta \\ \alpha\gamma \\ \beta\alpha \\ \beta\beta \\ \beta\gamma \end{bmatrix}$$

of energy levels to

$$\begin{bmatrix} \alpha\gamma \\ \alpha\beta \\ \alpha\alpha \\ \beta\gamma \\ \beta\beta \\ \beta\alpha \end{bmatrix}$$

and the general matrix

$$M = \begin{bmatrix} M_{11} & M_{12} & M_{13} & M_{14} & M_{15} & M_{16} \\ M_{21} & M_{22} & M_{23} & M_{24} & M_{25} & M_{26} \\ M_{31} & M_{32} & M_{33} & M_{34} & M_{35} & M_{36} \\ M_{41} & M_{42} & M_{43} & M_{44} & M_{45} & M_{46} \\ M_{51} & M_{52} & M_{53} & M_{54} & M_{55} & M_{56} \\ M_{61} & M_{62} & M_{63} & M_{64} & M_{65} & M_{66} \end{bmatrix}$$

is mapped to

$$\tilde{M} = \begin{bmatrix} M_{33} & M_{32} & M_{31} & M_{36} & M_{35} & M_{34} \\ M_{23} & M_{22} & M_{21} & M_{26} & M_{25} & M_{24} \\ M_{13} & M_{12} & M_{11} & M_{16} & M_{15} & M_{14} \\ M_{63} & M_{62} & M_{61} & M_{66} & M_{65} & M_{64} \\ M_{53} & M_{52} & M_{51} & M_{56} & M_{55} & M_{54} \\ M_{43} & M_{42} & M_{41} & M_{46} & M_{45} & M_{44} \end{bmatrix}.$$

In particular, all spin operators are given in the tilde basis as

$$\begin{aligned} \tilde{S}_z = S_z &= \frac{1}{2} \begin{bmatrix} 1 & & & & & \\ & 1 & & & & \\ & & 1 & & & \\ & & & -1 & & \\ & & & & -1 & \\ & & & & & -1 \end{bmatrix}, \tilde{I}_z = -I_z = \begin{bmatrix} -1 & & & & & \\ & 0 & & & & \\ & & 1 & & & \\ & & & -1 & & \\ & & & & 0 & \\ & & & & & 1 \end{bmatrix}, \tilde{S}_x = S_x \\ &= \frac{1}{2} \begin{bmatrix} 0 & 0 & 0 & 1 & 0 & 0 \\ 0 & 0 & 0 & 0 & 1 & 0 \\ 0 & 0 & 0 & 0 & 0 & 1 \\ 1 & 0 & 0 & 0 & 0 & 0 \\ 0 & 1 & 0 & 0 & 0 & 0 \\ 0 & 0 & 1 & 0 & 0 & 0 \end{bmatrix}, \tilde{I}_x = I_x \\ &= \frac{1}{\sqrt{2}} \begin{bmatrix} 0 & 1 & 0 & 0 & 0 & 0 \\ 1 & 0 & 1 & 0 & 0 & 0 \\ 0 & 1 & 0 & 0 & 0 & 0 \\ 0 & 0 & 0 & 0 & 1 & 0 \\ 0 & 0 & 0 & 1 & 0 & 1 \\ 0 & 0 & 0 & 0 & 1 & 0 \end{bmatrix}, \tilde{I}_y = -I_y, \tilde{S}_y = S_y. \quad (\text{A2}) \end{aligned}$$

Here, double-square brackets $[[\cdot]]$ denote a diagonal matrix with the given diagonal entries.

Appendix 3. Definition of the fictitious spin-1/2 operators

The spin operators defined in the Section A2 can be decomposed into fictitious spin-1/2 operators

$$\tilde{S}_z = I_z^{1-4} + I_z^{2-5} + I_z^{3-6}, \quad (\text{A3})$$

$$\tilde{I}_z = 2(-I_z^{1-2} - I_z^{2-3} - I_z^{4-5} - I_z^{5-6}), \quad (\text{A4})$$

$$\tilde{S}_x = (I_x^{1-4} + I_x^{2-5} + I_x^{3-6}), \quad (\text{A5})$$

$$\tilde{I}_x = \sqrt{2}(I_x^{1-2} + I_x^{2-3} + I_x^{4-5} + I_x^{5-6}). \quad (\text{A6})$$

$$\tilde{I}_z^2 = (2(-I_z^{1-2} - I_z^{2-3} - I_z^{4-5} - I_z^{5-6}))^2 \quad (\text{A7})$$

$$\tilde{S}_y = I_y^{1-4} + I_y^{2-5} + I_y^{3-6} \quad (\text{A8})$$

using the definitions of the fictitious spin-1/2 operators

$$I_z^{1-4} = \begin{bmatrix} \begin{bmatrix} \frac{1}{2} \\ 0 \\ 0 \end{bmatrix} \\ -\frac{1}{2} \\ 0 \\ 0 \end{bmatrix}, I_z^{2-5} = \begin{bmatrix} \begin{bmatrix} 0 \\ \frac{1}{2} \\ 0 \end{bmatrix} \\ 0 \\ -\frac{1}{2} \\ 0 \end{bmatrix}, I_z^{3-6} = \begin{bmatrix} \begin{bmatrix} 0 \\ 0 \\ \frac{1}{2} \end{bmatrix} \\ 0 \\ 0 \\ -\frac{1}{2} \end{bmatrix},$$

$$I_z^{1-2} = \begin{bmatrix} \begin{bmatrix} \frac{1}{2} \\ -\frac{1}{2} \end{bmatrix} \\ 0 \\ 0 \\ 0 \end{bmatrix}, I_z^{2-3} = \begin{bmatrix} \begin{bmatrix} 0 \\ \frac{1}{2} \\ -\frac{1}{2} \end{bmatrix} \\ 0 \\ 0 \\ 0 \end{bmatrix},$$

$$I_z^{4-5} = \begin{bmatrix} \begin{bmatrix} 0 \\ 0 \\ 0 \end{bmatrix} \\ \frac{1}{2} \\ -\frac{1}{2} \\ 0 \end{bmatrix}, I_z^{5-6} = \begin{bmatrix} \begin{bmatrix} 0 \\ 0 \\ 0 \end{bmatrix} \\ 0 \\ \frac{1}{2} \\ -\frac{1}{2} \end{bmatrix}$$

$$I_x^{1-4} = \begin{bmatrix} 0 & 0 & 0 & \frac{1}{2} & 0 & 0 \\ 0 & 0 & 0 & 0 & 0 & 0 \\ 0 & 0 & 0 & 0 & 0 & 0 \\ \frac{1}{2} & 0 & 0 & 0 & 0 & 0 \\ 0 & 0 & 0 & 0 & 0 & 0 \\ 0 & 0 & 0 & 0 & 0 & 0 \end{bmatrix},$$

$$I_x^{2-5} = \begin{bmatrix} 0 & 0 & 0 & 0 & 0 & 0 \\ 0 & 0 & 0 & 0 & \frac{1}{2} & 0 \\ 0 & 0 & 0 & 0 & 0 & 0 \\ 0 & 0 & 0 & 0 & 0 & 0 \\ 0 & \frac{1}{2} & 0 & 0 & 0 & 0 \\ 0 & 0 & 0 & 0 & 0 & 0 \end{bmatrix},$$

$$I_x^{3-6} = \begin{bmatrix} 0 & 0 & 0 & 0 & 0 & 0 \\ 0 & 0 & 0 & 0 & 0 & 0 \\ 0 & 0 & 0 & 0 & 0 & \frac{1}{2} \\ 0 & 0 & 0 & 0 & 0 & 0 \\ 0 & 0 & 0 & 0 & 0 & 0 \\ 0 & 0 & \frac{1}{2} & 0 & 0 & 0 \end{bmatrix},$$

$$I_y^{1-4} = \begin{bmatrix} 0 & 0 & 0 & -\frac{i}{2} & 0 & 0 \\ 0 & 0 & 0 & 0 & 0 & 0 \\ 0 & 0 & 0 & 0 & 0 & 0 \\ \frac{i}{2} & 0 & 0 & 0 & 0 & 0 \\ 0 & 0 & 0 & 0 & 0 & 0 \\ 0 & 0 & 0 & 0 & 0 & 0 \end{bmatrix},$$

$$I_y^{2-5} = \begin{bmatrix} 0 & 0 & 0 & 0 & 0 & 0 \\ 0 & 0 & 0 & 0 & -\frac{i}{2} & 0 \\ 0 & 0 & 0 & 0 & 0 & 0 \\ 0 & 0 & 0 & 0 & 0 & 0 \\ 0 & \frac{i}{2} & 0 & 0 & 0 & 0 \\ 0 & 0 & 0 & 0 & 0 & 0 \end{bmatrix},$$

$$I_y^{3-6} = \begin{bmatrix} 0 & 0 & 0 & 0 & 0 & 0 \\ 0 & 0 & 0 & 0 & 0 & 0 \\ 0 & 0 & 0 & 0 & 0 & -\frac{i}{2} \\ 0 & 0 & 0 & 0 & 0 & 0 \\ 0 & 0 & 0 & 0 & 0 & 0 \\ 0 & 0 & \frac{i}{2} & 0 & 0 & 0 \end{bmatrix},$$

$$I_x^{1-2} = \begin{bmatrix} 0 & \frac{1}{2} & 0 & 0 & 0 & 0 \\ \frac{1}{2} & 0 & 0 & 0 & 0 & 0 \\ 0 & 0 & 0 & 0 & 0 & 0 \\ 0 & 0 & 0 & 0 & 0 & 0 \\ 0 & 0 & 0 & 0 & 0 & 0 \\ 0 & 0 & 0 & 0 & 0 & 0 \end{bmatrix},$$

$$I_x^{2-3} = \begin{bmatrix} 0 & 0 & 0 & 0 & 0 & 0 \\ 0 & 0 & \frac{1}{2} & 0 & 0 & 0 \\ 0 & \frac{1}{2} & 0 & 0 & 0 & 0 \\ 0 & 0 & 0 & 0 & 0 & 0 \\ 0 & 0 & 0 & 0 & 0 & 0 \\ 0 & 0 & 0 & 0 & 0 & 0 \end{bmatrix},$$

$$I_x^{4-5} = \begin{bmatrix} 0 & 0 & 0 & 0 & 0 & 0 \\ 0 & 0 & 0 & 0 & 0 & 0 \\ 0 & 0 & 0 & 0 & 0 & 0 \\ 0 & 0 & 0 & 0 & \frac{1}{2} & 0 \\ 0 & 0 & 0 & \frac{1}{2} & 0 & 0 \\ 0 & 0 & 0 & 0 & 0 & 0 \end{bmatrix},$$

$$I_x^{5-6} = \begin{bmatrix} 0 & 0 & 0 & 0 & 0 & 0 \\ 0 & 0 & 0 & 0 & 0 & 0 \\ 0 & 0 & 0 & 0 & 0 & 0 \\ 0 & 0 & 0 & 0 & 0 & \frac{1}{2} \\ 0 & 0 & 0 & 0 & \frac{1}{2} & 0 \\ 0 & 0 & 0 & 0 & 0 & 0 \end{bmatrix}.$$

We rewrite the hyperfine and the quadrupole term using the fictitious spin-1/2 operator formalism:

$$\begin{aligned} A\tilde{S}_z\tilde{I}_z &= A(I_z^{1-4} + I_z^{2-5} + I_z^{3-6}) \\ &\quad \times (-2I_z^{1-2} - 2I_z^{2-3} - 2I_z^{4-5} - 2I_z^{5-6}) \\ &= 2A \left(\frac{1}{2} \begin{bmatrix} 1 \\ 0 \\ 0 \\ -1 \\ 0 \\ 0 \end{bmatrix} + \frac{1}{2} \begin{bmatrix} 0 \\ 1 \\ 0 \\ 0 \\ -1 \\ 0 \end{bmatrix} + \frac{1}{2} \begin{bmatrix} 0 \\ 0 \\ 1 \\ 0 \\ 0 \\ -1 \end{bmatrix} \right) \\ &\quad \cdot \left(-\frac{1}{2} \begin{bmatrix} 1 \\ -1 \\ 0 \\ 0 \\ 0 \\ 0 \end{bmatrix} - \frac{1}{2} \begin{bmatrix} 0 \\ 1 \\ -1 \\ 0 \\ 0 \\ 0 \end{bmatrix} - \frac{1}{2} \begin{bmatrix} 0 \\ 0 \\ 1 \\ 1 \\ -1 \\ 0 \end{bmatrix} \right. \\ &\quad \left. - \frac{1}{2} \begin{bmatrix} 0 \\ 0 \\ 0 \\ 1 \\ -1 \end{bmatrix} \right) = 2A \left(\frac{1}{2} \begin{bmatrix} 1 \\ 1 \\ 1 \\ -1 \\ -1 \end{bmatrix} \right) \\ &\quad \cdot \left(-\frac{1}{2} \begin{bmatrix} 1 \\ 0 \\ -1 \\ 1 \\ 0 \\ -1 \end{bmatrix} \right) = A \left(\begin{bmatrix} -1/2 \\ 0 \\ 1/2 \\ 1/2 \\ 0 \\ -1/2 \end{bmatrix} \right) \\ &= A(-I_z^{1-4} + I_z^{3-6}) \end{aligned}$$

and

$$\begin{aligned} \omega_Q &\left(\frac{3}{2} I_z^2 - \mathbb{1} \right) \\ &= \omega_Q \left(\frac{3}{2} (-2I_z^{1-2} - 2I_z^{2-3} - 2I_z^{4-5} - 2I_z^{5-6})^2 - \mathbb{1} \right) \\ &= \frac{3}{2} \omega_Q \left(\begin{bmatrix} -1 \\ 0 \\ 1 \\ -1 \\ 0 \\ 1 \end{bmatrix}^2 - \begin{bmatrix} 1 \\ 1 \\ 1 \\ 1 \\ 1 \\ 1 \end{bmatrix} \right) = \omega_Q \left(\begin{bmatrix} 1/2 \\ -1 \\ 1/2 \\ 1/2 \\ -1 \\ 1/2 \end{bmatrix} \right) \\ &= \omega_Q (I_z^{1-2} - I_z^{2-3} + I_z^{4-5} - I_z^{5-6}). \end{aligned}$$

Appendix 4. Definition of the unitary transformation $U(\theta_\gamma, \theta_\beta, \theta_\alpha)$

In section 3.1, we diagonalise the electronic part of the Hamiltonian (3) individually for each electronic manifold. The transformation matrix U is found by recalling the rotation rules

$e^{-i\theta A} B e^{i\theta A} = B \cos \theta - i[A, B] \sin \theta$ for angular momentum operators A, B and considering the components of the individual manifolds in (3) and the commutator $[A, B] = AB - BA$. The z direction of the tilted frame, in which the electronic part of the Hamiltonian is diagonal, is defined by the effective field direction of each manifold. For example considering the case of the γ manifold, the single transition [1–4] operators I_x^{1-4} , I_y^{1-4} , and I_z^{1-4} in the tilted frame are related to the I_x^{1-4} , I_y^{1-4} , and I_z^{1-4} operators by a rotation around the x axis with rotation angle θ_γ with $\cos \theta_\gamma = (\Delta\omega_e - A)/\omega_\gamma$ and $\sin \theta_\gamma = \omega_{1e}/\omega_\gamma$, c.f. Figure 2.

Overall, the unitary matrix U that diagonalises the electronic part of the Hamiltonian is given by

$$U(\theta_\gamma, \theta_\beta, \theta_\alpha) = U_x^{1-4}(\theta_\gamma) U_x^{2-5}(\theta_\beta) U_x^{3-6}(\theta_\alpha) \quad (\text{A9})$$

and

$$\begin{aligned} U(\theta_\gamma, \theta_\beta, \theta_\alpha) &= e^{-i\theta_\gamma I_x^{1-4}} e^{-i\theta_\beta I_x^{2-5}} e^{-i\theta_\alpha I_x^{3-6}} \\ &= \begin{bmatrix} \cos \frac{\theta_\gamma}{2} & 0 & 0 & -i \sin \frac{\theta_\gamma}{2} & 0 & 0 \\ 0 & 1 & 0 & 0 & 0 & 0 \\ 0 & 0 & 1 & 0 & 0 & 0 \\ -i \sin \frac{\theta_\gamma}{2} & 0 & 0 & \cos \frac{\theta_\gamma}{2} & 0 & 0 \\ 0 & 0 & 0 & 0 & 1 & 0 \\ 0 & 0 & 0 & 0 & 0 & 1 \end{bmatrix} \\ &\times \begin{bmatrix} 1 & 0 & 0 & 0 & 0 & 0 \\ 0 & \cos \frac{\theta_\beta}{2} & 0 & 0 & -i \sin \frac{\theta_\beta}{2} & 0 \\ 0 & 0 & 1 & 0 & 0 & 0 \\ 0 & 0 & 0 & 1 & 0 & 0 \\ 0 & -i \sin \frac{\theta_\beta}{2} & 0 & 0 & \cos \frac{\theta_\beta}{2} & 0 \\ 0 & 0 & 0 & 0 & 0 & 1 \end{bmatrix} \\ &\times \begin{bmatrix} 1 & 0 & 0 & 0 & 0 & 0 \\ 0 & 1 & 0 & 0 & 0 & 0 \\ 0 & 0 & \cos \frac{\theta_\alpha}{2} & 0 & 0 & -i \sin \frac{\theta_\alpha}{2} \\ 0 & 0 & 0 & 1 & 0 & 0 \\ 0 & 0 & 0 & 0 & 1 & 0 \\ 0 & 0 & -i \sin \frac{\theta_\alpha}{2} & 0 & 0 & \cos \frac{\theta_\alpha}{2} \end{bmatrix} \\ &= \begin{bmatrix} \cos \frac{\theta_\gamma}{2} & 0 & 0 & 0 & 0 & 0 \\ 0 & \cos \frac{\theta_\beta}{2} & 0 & 0 & 0 & 0 \\ 0 & 0 & \cos \frac{\theta_\alpha}{2} & 0 & 0 & 0 \\ -i \sin \frac{\theta_\gamma}{2} & 0 & 0 & 0 & 0 & 0 \\ 0 & -i \sin \frac{\theta_\beta}{2} & 0 & 0 & 0 & 0 \\ 0 & 0 & -i \sin \frac{\theta_\alpha}{2} & 0 & 0 & 0 \end{bmatrix} \end{aligned}$$

$$\begin{bmatrix} -i \sin \frac{\theta_\gamma}{2} & 0 & 0 \\ 0 & -i \sin \frac{\theta_\beta}{2} & 0 \\ 0 & 0 & -i \sin \frac{\theta_\alpha}{2} \\ \cos \frac{\theta_\gamma}{2} & 0 & 0 \\ 0 & \cos \frac{\theta_\beta}{2} & 0 \\ 0 & 0 & \cos \frac{\theta_\alpha}{2} \end{bmatrix} \quad (\text{A10})$$

Each individual matrix was built according to the properties of rotation operators [38], here specifically $\exp(-iS_x\theta) = 1 \cos \theta/2 - i2S_x \sin \theta/2$ and we have used $S_x = \tilde{S}_x$ from A1.

Appendix 5. Selective $\pi/2$ excitation on EPR 3–6 (α)

We start with the equilibrium density matrix

$$\rho(0) = -RI_z^{1-4} - RI_z^{2-5} - RI_z^{3-6}$$

and apply a MW $(\pi/2)_x$ pulse selective on the α manifold. According to the transformation $U\rho(0)U^{-1}$ with the propagator $U(\theta_\gamma, \theta_\beta, \theta_\alpha)$ from equation (A10) and setting $\theta_\alpha = \frac{\pi}{2}$, $\theta_\beta = 0$, and $\theta_\gamma = 0$, we obtain the density matrix in the doubly rotating frame after a selective $\pi/2$ excitation:

$$\begin{aligned} \rho(0^+) &= e^{-i\frac{\pi}{2} I_x^{3-6}} \{-RI_z^{1-4} - RI_z^{2-5} - RI_z^{3-6}\} e^{i\frac{\pi}{2} I_x^{3-6}} \\ &= -R \cos \frac{\pi}{2} I_z^{3-6} + R \sin \frac{\pi}{2} I_y^{3-6} - RI_z^{2-5} - RI_z^{1-4} \\ &= -RI_z^{1-4} - RI_z^{2-5} + RI_y^{3-6} \end{aligned}$$

Appendix 6. Polarisation transfer during CP for EPR γ and EPR β

EPR 2–5 (β):

When EPR excitation occurs, e.g. selectively on the β transition by means of a MW $(\frac{\pi}{2})_x$ pulse, the initial density matrix $\rho(0^+)$ in the doubly rotating frame becomes

$$\begin{aligned} \rho(0^+) &= e^{-i\frac{\pi}{2} I_x^{2-5}} \{-RI_z^{1-4} - RI_z^{2-5} - RI_z^{3-6}\} e^{i\frac{\pi}{2} I_x^{2-5}} \\ &= -RI_z^{1-4} + RI_y^{2-5} - RI_z^{3-6} \end{aligned}$$

which is subsequently transformed to the tilted frame of the β manifold via the transformation $\rho'(0^+) = U\rho(0^+)U^{-1}$ and $U = U_x(\theta_\gamma, \theta_\beta, \theta_\alpha)$ defined in A4. The angles for $|A| \gg \omega_{1e}$ (malonic acid) are given in Table 1 as $\theta_\alpha = \pi$, $\theta_\beta = \frac{\pi}{2}$, and $\theta_\gamma = 0$:

$$\rho'(0^+) = \begin{bmatrix} -R/2 \\ R/2 \\ R/2 \\ R/2 \\ -R/2 \\ -R/2 \end{bmatrix}$$

The eNCP process equalises the populations of degenerate energy levels and we obtain for CP[1'–2'], CP[2'–6'], CP[3'–5'],

and CP[4'-5'] the density matrices

$$\rho'(t_{\text{CP}}^{1-2}) = \begin{bmatrix} 0 \\ 0 \\ R/2 \\ R/2 \\ -R/2 \\ -R/2 \end{bmatrix}, \quad \rho'(t_{\text{CP}}^{2-6}) = \begin{bmatrix} -R/2 \\ 0 \\ R/2 \\ R/2 \\ -R/2 \\ 0 \end{bmatrix},$$

$$\rho'(t_{\text{CP}}^{3-5}) = \begin{bmatrix} -R/2 \\ R/2 \\ 0 \\ R/2 \\ 0 \\ -R/2 \end{bmatrix}, \quad \rho'(t_{\text{CP}}^{4-5}) = \begin{bmatrix} -R/2 \\ R/2 \\ 0 \\ 0 \\ 0 \\ -R/2 \end{bmatrix}.$$

After transforming back into the doubly rotating frame $\rho(t_{\text{CP}}) = U^{-1} \rho'(t_{\text{CP}}^{[i'-j']}) U$ and neglecting off-diagonal elements, we obtain the density matrices

$$\rho(t_+^{1-2}) = \begin{bmatrix} 0 \\ -R/4 \\ -R/2 \\ R/2 \\ -R/4 \\ R/2 \end{bmatrix}, \quad \rho(t_+^{2-6}) = \begin{bmatrix} -R/2 \\ -R/4 \\ 0 \\ R/2 \\ -R/4 \\ R/2 \end{bmatrix},$$

$$\rho(t_+^{3-5}) = \begin{bmatrix} -R/2 \\ R/4 \\ -R/2 \\ R/2 \\ R/4 \\ 0 \end{bmatrix}, \quad \rho(t_+^{4-5}) = \begin{bmatrix} -R/2 \\ -R/2 \\ -R/2 \\ 0 \\ R/4 \\ R/2 \end{bmatrix}.$$

EPR 1-4 (γ):

When EPR excitation occurs, e.g. selectively on the γ transition by means of a MW $(\frac{\pi}{2})_x$ pulse, the initial density matrix $\rho(0^+)$ in the doubly rotating frame becomes

$$\begin{aligned} \rho(0^+) &= e^{-i\frac{\pi}{2} I_x^{1-4}} \{-RI_z^{1-4} - RI_z^{2-5} - RI_z^{3-6}\} e^{i\frac{\pi}{2} I_x^{1-4}} \\ &= +RI_y^{1-4} - RI_z^{2-5} - RI_z^{3-6} \end{aligned}$$

which is transformed to the tilted frame of the γ manifold via the transformation $\rho'(0^+) = U\rho(0^+)U^{-1}$ and $U = U_x(\theta_\gamma, \theta_\beta, \theta_\alpha)$ defined in A4. The angles for $|A| \gg \omega_{1e}$ (malonic acid) are (see Table 1) $\theta_\alpha = \pi$, $\theta_\beta = \pi$, and $\theta_\gamma = \pi/2$:

$$\rho'(0^+) = \begin{bmatrix} R/2 \\ R/2 \\ R/2 \\ -R/2 \\ -R/2 \\ -R/2 \end{bmatrix}$$

The eNCP process equalises the populations of the degenerate energy levels and for CP [1-5] and CP [2-4] (Table 2) we obtain

$$\rho'(t_{\text{CP}}^{1-5}) = \begin{bmatrix} 0 \\ R/2 \\ R/2 \\ -R/2 \\ 0 \\ -R/2 \end{bmatrix}, \quad \rho'(t_{\text{CP}}^{2-4}) = \begin{bmatrix} R/2 \\ 0 \\ R/2 \\ 0 \\ -R/2 \\ -R/2 \end{bmatrix}.$$

According to equation (8), transforming $\rho(t_{\text{CP}}) = U^{-1} \rho'(t_{\text{CP}}^{[i'-j']}) U$ back into the doubly rotating frame and neglecting off-diagonal elements leads to the density matrices

$$\rho(t_+^{2-4}) = \begin{bmatrix} R/4 \\ -R/2 \\ -R/2 \\ R/4 \\ 0 \\ R/2 \end{bmatrix}, \quad \rho(t_+^{1-5}) = \begin{bmatrix} -R/4 \\ 0 \\ -R/2 \\ -R/4 \\ R/2 \\ R/2 \end{bmatrix}.$$

Appendix 7. eNCP simulation parameters

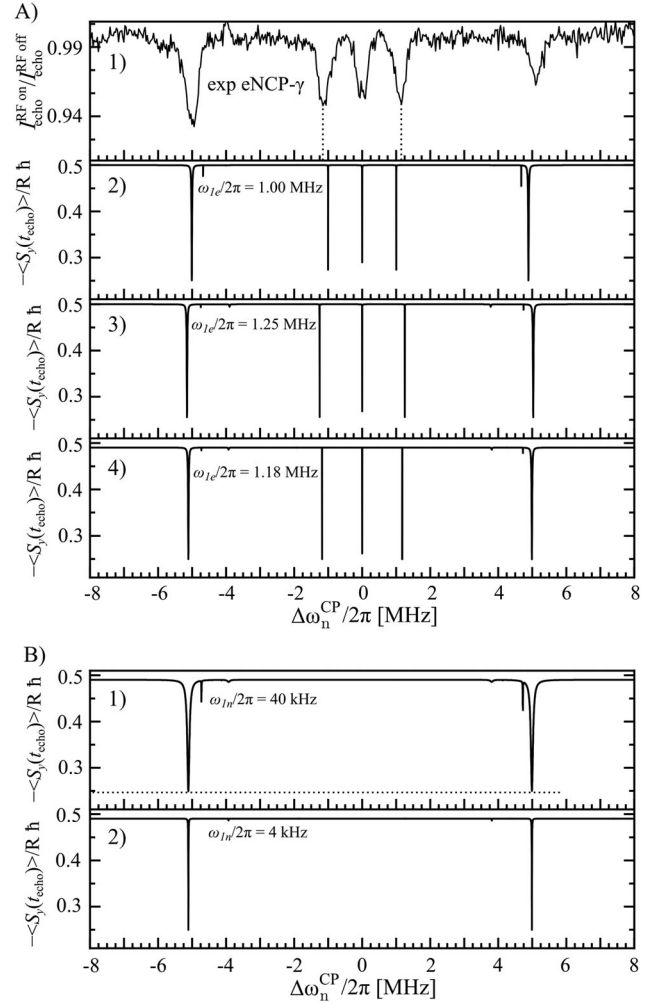


Figure A1. Comparison of the experimental eNCP spectrum recorded selectively on EPR γ and corresponding simulations by varying $\omega_{1e}/2\pi$ (A) and $\omega_{1n}/2\pi$ (B). *Exp. Conditions:* $\nu_{\text{EPR}} = 94$ GHz, shot repetition time = 100 ms; $t_{\pi/2, \text{mw}} = 200$ ns, $t_{\text{CP}} = 150$ μ s, one shot/point, random RF acquisition, 100–250 scans. *Simulation parameters:* (A2) $t_{\pi/2, \text{mw}} = 250$ ns, $\omega_{1e}/2\pi = 1.00$ MHz, $\omega_{1n}/2\pi = 10$ kHz; (A3) $t_{\pi/2, \text{mw}} = 200$ ns, $\omega_{1e}/2\pi = 1.25$ MHz, $\omega_{1n}/2\pi = 10$ kHz; (A4) $t_{\pi/2, \text{mw}} = 200$ ns, $\omega_{1e}/2\pi = 1.18$ MHz, $\omega_{1n}/2\pi = 10$ kHz; (B1) $t_{\pi/2, \text{mw}} = 200$ ns, $\omega_{1e}/2\pi = 1.18$ MHz, $\omega_{1n}/2\pi = 40$ kHz; (B2) $t_{\pi/2, \text{mw}} = 200$ ns, $\omega_{1e}/2\pi = 1.18$ MHz, $\omega_{1n}/2\pi = 4$ kHz.

Appendix 8. Davies ENDOR experiment and simulations

We start by shortly summarising the structure of the Davies-ENDOR pulse sequence (Figure A2, A). Two MW channels with the same phase but different amplitudes were employed. The amplitude of the first MW channel was adjusted to deliver a selective inversion pulse of $t_\pi = 400$ ns. A RF read-out π pulse of $25 \mu\text{s}$ was set with a delay of approx. $1 \mu\text{s}$ following the MW inversion pulse. The frequency of this pulse was stochastically swept over the ENDOR frequency range using one acquisition shot per RF (1 shot/point). A non-selective MW detection sequence of the form $t_{\pi/2} - \tau - t_\pi$ and with $t_\pi = 60$ ns was applied on the second MW channel at an approximate delay time of $1 \mu\text{s}$ following the ENDOR RF pulse.

We performed standard Davies ENDOR experiments and simulations as a control for the new experiments and simulations. The core of our Davies simulation routine is very similar to the CP-ENDOR simulation. However, the eNCP step is replaced by a selective microwave pulse, similar as for the experimental procedure. The simulated ENDOR effect is consistent with the theoretical expectation [9] of $\frac{\langle S_z \rangle}{3}$ or $0.5 \cdot R$. Here, some asymmetry of the experimentally observed ENDOR peaks is evident (Figure A2). This asymmetry can be reproduced by considering the so-called hf enhancement factor [35] in the simulation with *Easyspin* [36] (Figure A3). This factor, however, is not considered in our Davies simulation routine (Figure A2), thus lines are predicted to have equal intensities of $1/2 R$.

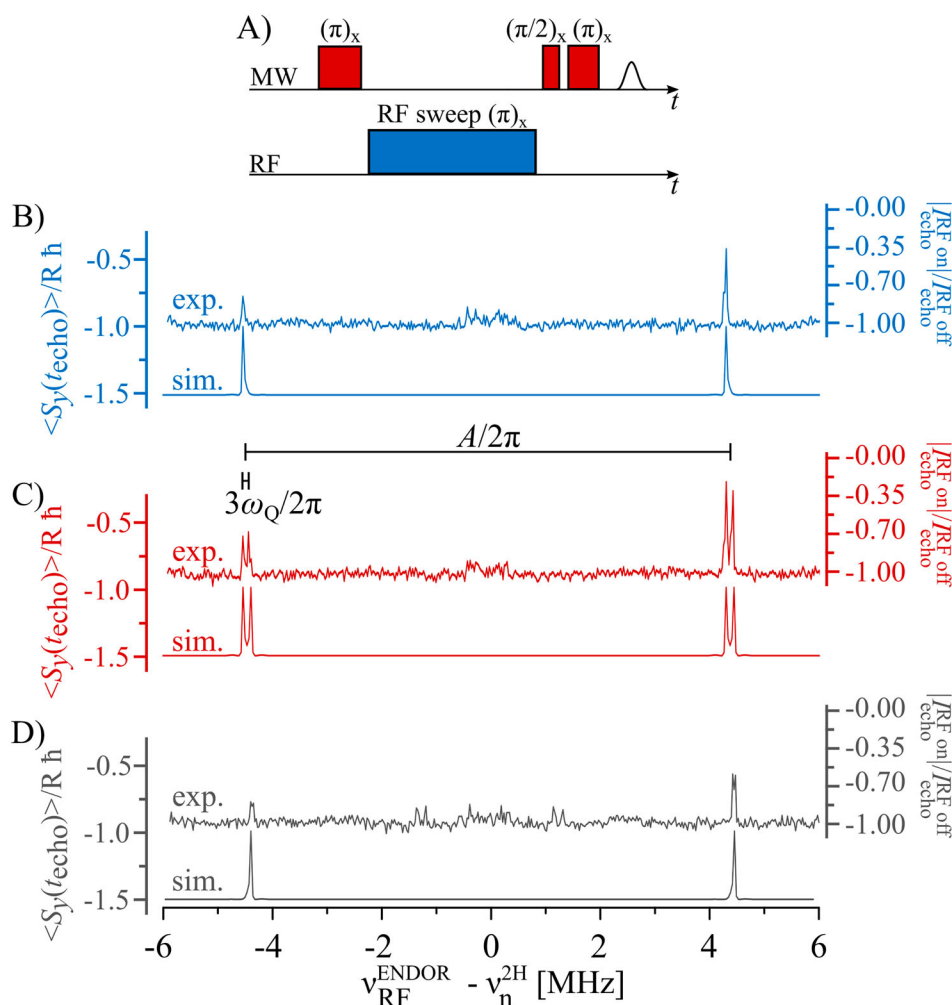


Figure A2. (A) Schematic pulse sequence for Davies ENDOR. EPR line selective Davies ENDOR spectra and simulations (EPR α (B), EPR β (C), and EPR γ (D)) plotted in the convenient ENDOR frequency domain. *Exp. Conditions:* $\nu_{\text{EPR}} = 94$ GHz, $t_{\pi, \text{mw}, \text{prep}} = 400$ ns, $t_{\text{ENDOR}} = 25 \mu\text{s}$, $t_{\pi, \text{mw}, \text{detect}} = 60$ ns, shot repetition time = 100 ms, 1 shot/point, random RF acquisition, 20 scans each. *Sim. parameters:* $\omega_{1e}/2\pi = 1.25$ MHz, $\omega_{1n}/2\pi = 13$ kHz, $A/2\pi = -8.9$ MHz, $\omega_Q/2\pi = -0.04$ MHz, $\Delta\omega_e = \pm A/2\pi$, 0 MHz.

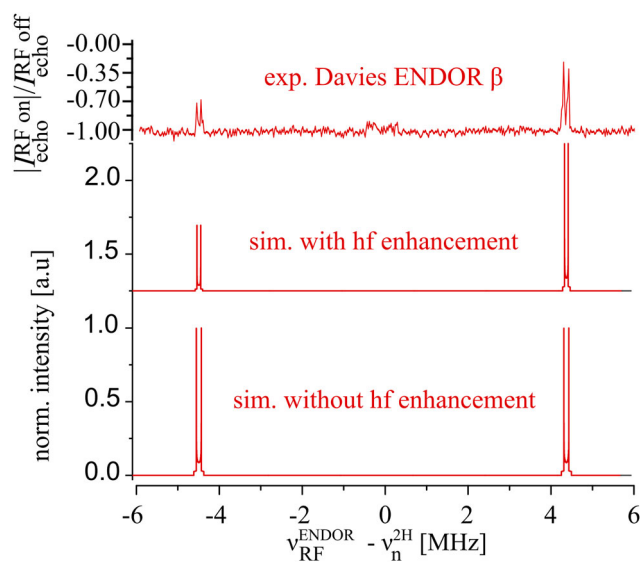


Figure A3. Davies ENDOR spectrum with selective excitation on EPR β and *EasySpin* simulations with and without considering the hf-enhancement factor. *Exp. Conditions:* $\nu_{\text{EPR}} = 94$ GHz, $t_{\pi, \text{mw}, \text{prep}} = 400$ ns, $t_{\text{ENDOR}} = 25$ μ s, $t_{\pi, \text{mw}, \text{detect}} = 60$ ns, shot repetition time = 100 ms, 1 shot/point, random rf acquisition, 20 scans each. *Sim. parameters:* $\nu_{\text{EPR}} = 94$ GHz, $g_e = 2.0023$, $A/2\pi = -8.9$ MHz, $\omega_Q/2\pi = -0.04$ MHz, $\Delta\omega_e = 0$ MHz. *EasySpin* simulations were performed using the 'salt' routine and full matrix diagonalization.

Appendix 9. CP-ENDOR experimental and theoretical results for EPR γ

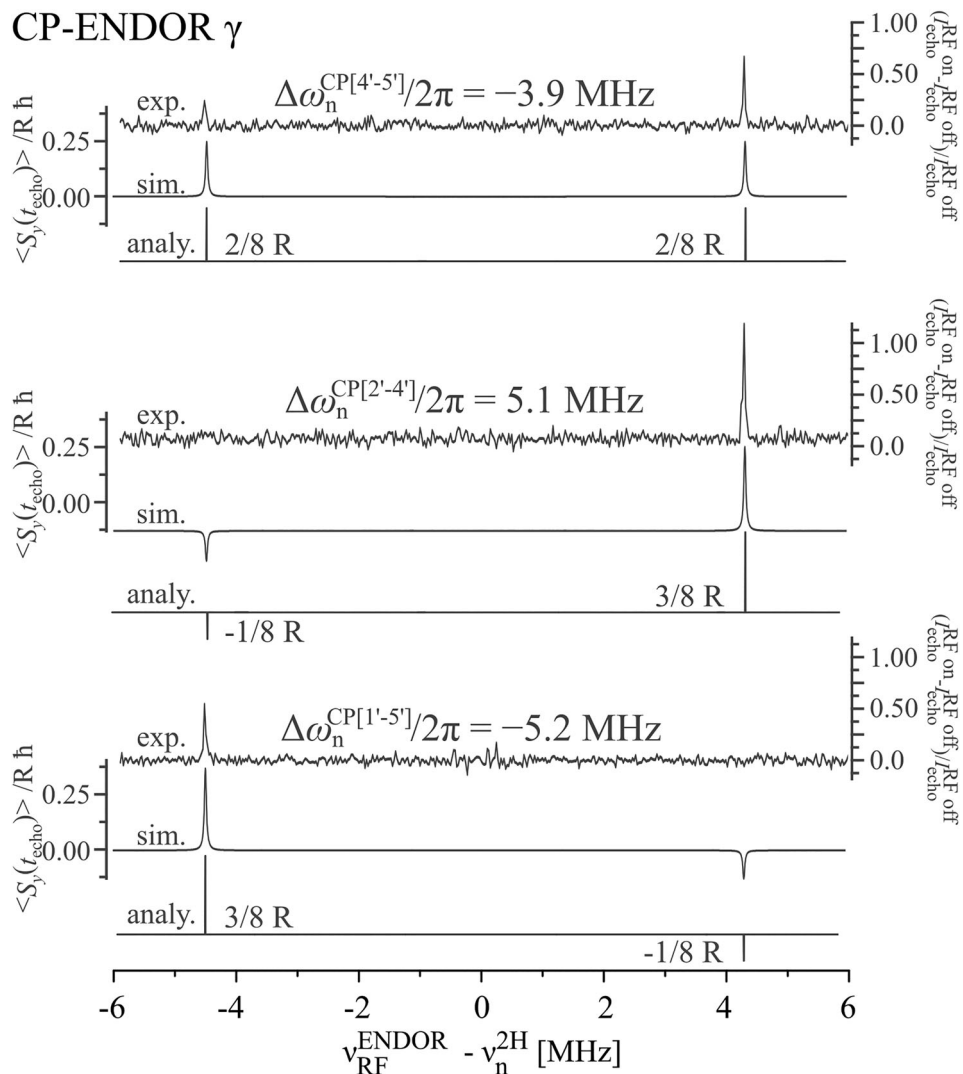


Figure A4. Experimental CP-ENDOR spectra on a deuterated malonic-acid single crystal, numerical CP-ENDOR simulations, and peak intensities according to our analytical solutions plotted in the ENDOR convenient frequency domain. Results are shown for the selective excitation of the EPR γ transition. *Exp. Conditions:* $\nu_{\text{EPR}} = 94$ GHz, $t_{\pi/2, \text{MW}} = 200$ ns, $\omega_{1e}/2\pi = 1.25$ MHz, $t_{\text{CP}} = 150$ μ s, $t_{\text{ENDOR}} = 25$ μ s, shot repetition time = 100 ms, 1 shot/point, random RF acquisition, 100 scans each. *Sim. parameters:* $\omega_{1e}/2\pi = 1.18$ MHz, $\omega_{1n}/2\pi = 13$ kHz, $A/2\pi = -8.9$ MHz, $\omega_Q/2\pi = -0.04$ MHz, $\Delta\omega_e = \pm A/2\pi, 0$ MHz.